Constraining Upper Mantle Viscosity Using Temperature and Water Content Inferred from Seismic and Magnetotelluric Data

Enter authors here: F. Ramirez[1,2], K. Selway[1,2,3], C. P. Conrad[2], and C. Lithgow-Bertelloni[4]

[1]Department of Earth and Environmental Sciences, Macquarie University, Australia

[2]Centre for Earth Evolution and Dynamics, University of Oslo, Norway

[3]Future Industries Institute, University of South Australia

[4]Earth, Planetary, and Space Sciences, University of California, Los Angeles

Corresponding author: Florence Ramirez (f.d.c.ramirez@geo.uio.no)

Key Points:

- Mantle viscosity is often inferred from seismic velocity observations, which are sensitive to temperature but not water content
- We show that adding magnetotelluric observations (sensitive to water content) improves viscosity estimates
- Rock composition affects viscosity estimates through its effect on seismic velocity and electrical conductivity

Abstract

Mantle viscosity controls a variety of geodynamic processes such as glacial isostatic adjustment (GIA), but it is poorly constrained because it cannot be measured directly from geophysical measurements. Here we develop a method that calculates viscosity using empirical viscosity flow laws coupled with mantle parameters (temperature and water content) inferred from seismic and magnetotelluric (MT) observations. We find that combining geophysical constraints allows us to place significantly tighter bounds on viscosity estimates compared to using seismic or MT observations alone. In particular, electrical conductivity inferred from MT data can determine whether upper mantle minerals are hydrated, which is important for viscosity reduction. Additionally, we show that rock composition should be considered when estimating viscosity from geophysical data because composition directly affects seismic velocity and electrical conductivity. Therefore, unknown composition increases uncertainty in temperature and water content, and makes viscosity more uncertain. Furthermore, calculations that assume pure thermal control of seismic velocity may misinterpret compositional variations as temperature, producing erroneous interpretations of mantle temperature and viscosity. Stress and grain size also affect the viscosity and its associated uncertainty, particularly via their controls on deformation regime. Dislocation creep is associated with larger viscosity uncertainties than diffusion creep. Overall, mantle viscosity can be estimated best when both seismic and MT data are available and the mantle composition, grain size and stress can be estimated. Collecting additional MT data probably offers the greatest opportunity to improve geodynamic or GIA models that rely on viscosity estimates.

Plain Language Summary

Many geological processes depend on the viscosity of the upper mantle, which describes how easily the rocks can ‘flow’. The larger the viscosity of the upper mantle, the slower and/or harder it is for rocks to deform over geological timescales. Thus, constraining upper mantle viscosity would certainly help us to understand and even simulate many geodynamic processes, such as Earth’s surface response to past ice melting. Although mantle viscosity cannot be measured directly, rock deformation experiments tell us how viscosity depends on rock properties, many of which can be determined from geophysical observations. Here we develop a method that calculates mantle viscosity from estimates of temperature and water content inferred from seismic and magnetotelluric (MT) observations, respectively. We show that the combination of these two observations improves viscosity estimates compared to either observation alone. When estimating viscosity from seismic and MT data, rock composition has to be considered. Because rock composition directly affects the interpretation of geophysical observations, better knowledge of rock composition can greatly reduce uncertainty in viscosity estimates. Overall, we conclude that additional MT surveying could offer new opportunities to better constrain viscosity in regions where robust geodynamic modelling is needed.

1 Introduction

Mantle viscosity controls the pace of upper mantle dynamics, including rates for plate motions, subduction deformation, small-scale convection, and glacial isostatic adjustment (GIA) processes. In particular, upper mantle viscosity influences the rate of surface uplift and associated sea level change caused by GIA, which is the viscous response of the Earth to changes in ice mass. However, surface uplift rates measured by geodesy (e.g., GNSS) in places with modern-day ice sheets such as in Greenland and Antarctica additionally measure the instantaneous elastic response of the solid earth to modern-day deglaciation (e.g., Conrad & Hager, 1997; Mitrovica et al., 2001). Thus,

regional patterns of ground uplift and relative sea level (RSL) change depend on both the instantaneous elastic and long-term viscous components (e.g., Conrad, 2013). To accurately infer rates of ice loss in polar regions (e.g., Khan et al., 2016), the elastic and viscous contributions to the surface uplift must be separated from each other. Achieving this requires a robust GIA model, which unfortunately is usually not available in polar regions because of poorly-constrained mantle viscosity. This study aims to investigate how geophysical observations (independent of geodetic observations) can be used to calculate and constrain upper mantle viscosity.

Mantle viscosity is commonly constrained from observations of GIA-induced phenomena (e.g., RSL changes over time, temporal changes in Earth's gravitational field, and polar wander feedbacks) (e.g., Kaufmann & Lambeck, 2000; Peltier et al., 1978; Peltier, 2004). However, these calculations generally produce 1-D (layered) viscosity profiles defined by only a few viscosity layers due to the depth-insensitivity of GIA observables (e.g., Paulson et al., 2007) and because the ice-loading history are usually broad scale (100s to 1000s of km). This restricts us from inferring regional lateral variations in viscosity that may influence GIA observations (e.g., Paulson et al., 2005). Furthermore, such observations are geographically bound to places where ice history and RSL change are known. Similarly, mantle viscosities inferred from viscoelastic relaxation models for post-seismic deformation near subduction zones (e.g., Wang et al., 2012; Pollitz et al., 2008) are geographically constrained, data-limited, and frequency or time dependent that commonly results in lower values ($10^{17} - 10^{18}$) than the usual lower mantle viscosity bound (10^{19}). Hence, other sources of information, independent from any GIA observables and seismic events, that can place additional constraints on mantle viscosity are important. For instance, localized geophysical measurements, such as seismic and magnetotelluric (MT) observations, can be used to infer variations in mantle structure that also relate to mantle viscosity (e.g., Ivins et al., 2021; O'Donnell et al., 2017; Selway et al., 2020; Liu & Hasterok, 2016). Because such geophysical measurements scan the subsurface of the Earth, they can provide good depth and lateral resolution for upper mantle structure. However, systematic methods for converting seismic and MT observations into 3-D viscosity models require more development and the uncertainties associated with such conversions are poorly constrained.

Here we investigate the relationship between the empirically-determined rheology of mantle minerals and the mantle parameters that can be observed geophysically. From rock deformation experiments, olivine rheology is thought to be controlled primarily by temperature T, water fugacity f_{H2O}, grain size d, stress σ, partial melt φ, and pressure P (e.g., Hirth & Kohlstedt, 1996; Bercovici & Ricard, 2012; Karato & Jung, 2003) as described by the stress - strain rate $\dot{\epsilon}$ relationship for power law creep,

$$\dot{\epsilon} = A\sigma^n d^{-p} f_{H2O}^r \, exp\,(\alpha\varphi) \, exp\left(-\frac{E^* + PV^*}{RT}\right) \quad (1)$$

where E^* is the activation energy, V^* is the activation volume, R is the ideal gas constant, and A, p, n and r are all laboratory-derived parameters (e.g., Hirth & Kohlstedt, 2003). The stress - strain rate relationship may be linear ($n \sim 1$) or non-linear ($n > 1$) if the dominant deformation mechanism is diffusion (strongly grain size sensitive) or dislocation (strongly stress sensitive) creep, respectively. In either case, we define an effective viscosity as:

$$\eta_{eff} = \frac{\sigma}{\dot{\epsilon}_{tot}} \quad (2)$$

where σ is stress and $\dot{\epsilon}_{tot} = \dot{\epsilon}_{dis} + \dot{\epsilon}_{dif} + \dot{\epsilon}_{DisGBS}$ is the total strain rate contributed by the major plastic deformation mechanisms in olivine, here considered to be dislocation creep, diffusion

creep, and dislocation-accommodated grain boundary sliding, respectively. For non-linear cases ($n > 1$), the effective viscosity is stress-dependent.

Combining Equations (1) and (2), it is clear that the effective viscosity of mantle aggregates decreases with increasing temperature, water content and melt fraction. Thus, constraining these factors from geophysical observations can improve estimates of mantle viscosity. Temperature can be estimated from seismic (e.g., Goes et al., 2000; Lucas et al., 2020; Milne et al., 2018; Heezsel et al., 2016), MT (e.g., Selway et al., 2020) and heat flow (e.g., Artemieva, 2006) data. Indeed, seismic tomography models are widely used to infer mantle thermal structure (e.g., Goes et al., 2000; Lloyd et al., 2015), with the assumption that seismic velocity anomalies are mainly thermally-controlled (e.g., Ivins & Sammis, 1995). Many such studies neglect compositional effects that can influence seismic velocity (c.f., Lee, 2003; Shen et al., 2018; Xu et al., 2008; Fullea et al., 2021). Thus, variations in chemical composition (i.e., iron, magnesium, silica and calcium content) that affect the density and elastic moduli of the mantle rocks may be misinterpreted as thermal variations. In this case, inference of temperature from seismic observations may result in erroneous viscosity estimates.

MT images the Earth's electrical conductivity, which, in addition to being highly sensitive to temperature, is also sensitive to the presence of partial melt, conductive mineral phases and the water (hydrogen) content of nominally anhydrous minerals. Thus, the water content in nominally anhydrous olivine (as well as partial melt) can be quantified from MT if temperature is constrained (e.g., Yoshino et al., 2009). Estimates of viscosity may additionally depend on other factors such as partial melt, grain-size variations, or stresses. If present, partial melt will have a seismic and MT response (e.g., Chantel et al., 2016). By contrast, grain size in general cannot be directly inferred from geophysical observables, apart from its impact on seismic attenuation (e.g., Faul & Jackson, 2005). However, information on grain size can potentially be gained from mantle xenoliths (e.g., Ave Lallemant et al., 1980) and a region's tectonic history. The distribution of stresses can be inferred from numerical or analytical models (e.g., Stevens et al., 2016; Johnston et al., 1998) of tectonic activity or loading.

In this study, we develop a method to estimate upper mantle viscosity using a three-step process: (1) constrain temperature from seismic observations (after accounting for possible compositional variations); (2) constrain the water content from MT observations; and finally, (3) convert the calculated thermal and water content profiles into a viscosity structure using Eqs. (1) and (2). In each step, we assess and quantify the uncertainties such as those associated with the geophysical observations themselves. Using this method, we expect to develop geophysically-derived mantle viscosity models that will be particularly useful in polar regions where the GIA response is poorly constrained.

2 Set-up for constraining effective vsiscosity from geophysical constraints

To investigate how MT and seismic data can be used to constrain mantle viscosity, we consider a simplified, theoretical upper mantle region at depth z (e.g., target region in Fig. 1a) composed of a melt-free, pure olivine. First, we forward model absolute seismic velocities and electrical conductivities for pure olivine (Fo_{90}) at a range of temperatures T and water contents C_{OH} (Fig. 1b) at fixed pressure (or depth) using the Hacker and Abers (2004) approach for V_s and the water-

144 dependent formulation of Gardés et al. (2014) for conductivity. Then, we calculate effective

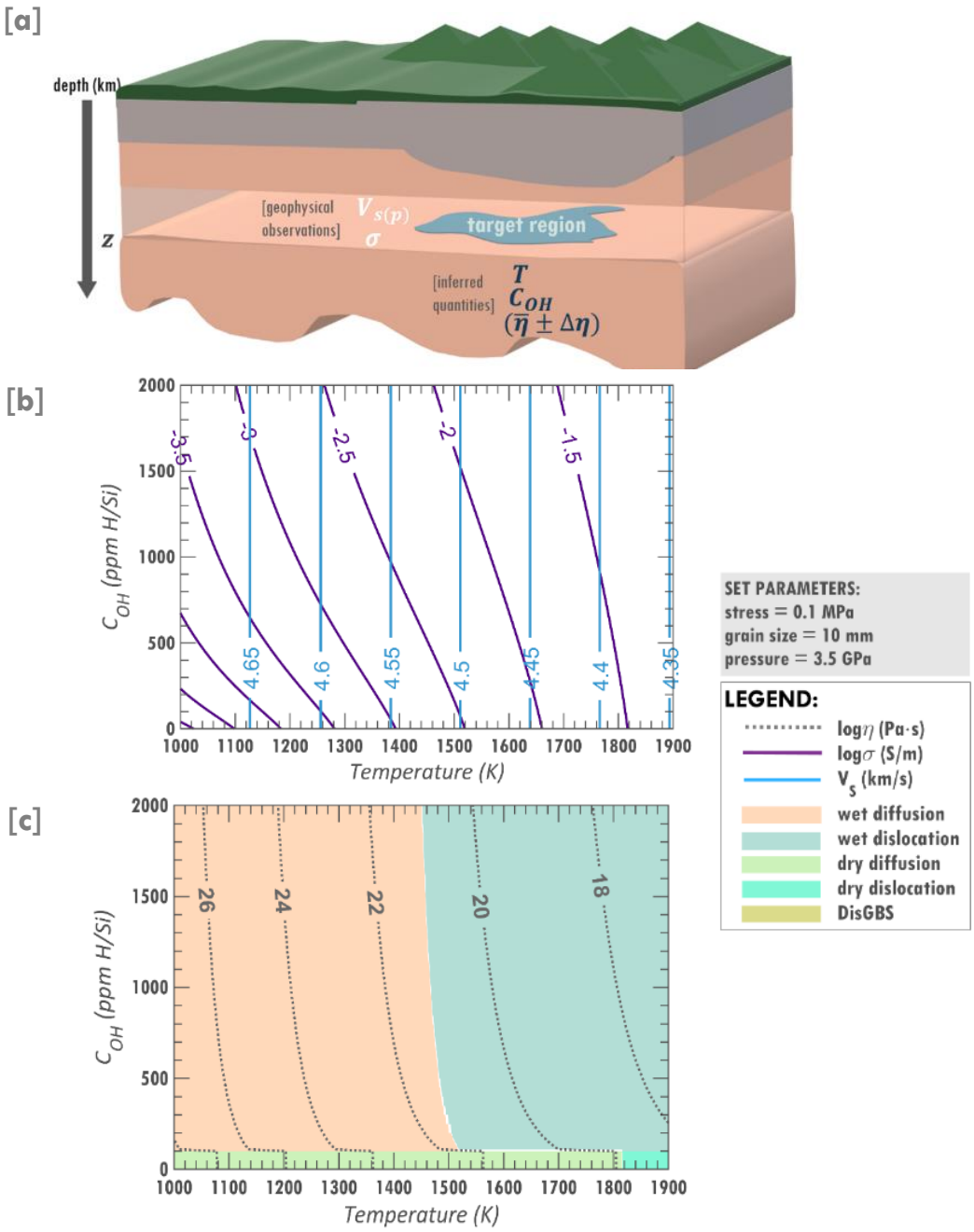

Figure 1. Inferring upper mantle viscosity from geophysical observations. [a] The set-up used in this study, where a melt-free region in the upper mantle has measured seismic velocity ($\boldsymbol{V_s}$) and MT-derived electrical conductivity ($\boldsymbol{\sigma}$). The temperature ($\boldsymbol{T}$) of this region is inferred from seismic velocity (neglecting compositional effects for now) and the water content ($\boldsymbol{C_{OH}}$) is constrained from electrical conductivity if $\boldsymbol{T}$ is known. Its effective viscosity is then determined by substituting the constrained $\boldsymbol{T}$ and $\boldsymbol{C_{OH}}$, under an assumed differential stress and olivine grain size, into Eqs. (1) and (2). **[b and c]** The deformation mechanism map for pure olivine over $\boldsymbol{C_{OH}}$ and $\boldsymbol{T}$ space with shear wave velocity (blue) and electrical conductivity (violet) contour lines in [b], and log of effective viscosity (dotted grey) contour lines in [c] for a single choice of stress, grain size and pressure. For a given geophysical observation (with uncertainty), the viscosity range can be estimated mathematically and visually by overlapping the contour lines from [b] onto [c].

viscosity η_{eff} as a function of temperature and water content (Fig. 1c) for a single choice of stress and grain size using Eqs. (1) and (2), where C_{OH} in ppm H/Si is converted into f_{H2O} (in MPa) using the Zhao et al. (2004) formulation. Thus, to estimate viscosity from geophysical observations, we can use seismically-derived V_s and MT-derived electrical conductivity models for a region to constrain a range of T and C_{OH} using Fig. 1b. Then, by combining Figs. 1b and c, we can determine an effective viscosity range whether we consider seismics only (section 2.1), MT only (section 2.2), or both (section 2.3).

The relationship between strain rate and stress, temperature, grain size, pressure and C_{OH} depends on the relative amplitudes of the different deformation mechanisms. The dominant mechanism (colored background, Fig. 1c) is that with the highest strain rate (lowest viscosity), and differs for dry (defined here as $C_{OH} \leq 100$ ppm H/Si (e.g., Mei & Kohlstedt, 2000a)) and wet ($C_{OH} > 100$ ppm H/Si) upper mantle conditions as well as variations in the other parameters.

2.1 Absolute seismic velocity and temperature

With the aid of thermodynamic analysis and laboratory-derived parameters, the absolute elastic seismic velocity of a rock at any temperature and pressure can be estimated from the seismic velocities of the constituent minerals using Voigt-Reuss-Hill averaging scheme. Figure 1b shows the absolute seismic velocities calculated using the Hacker and Abers (2004) approach for pure olivine as a function of C_{OH} and T. V_s plots as vertical contours because seismic velocities are commonly not sensitive to hydrogen content, unless the water content is very large that may significantly reduce the elastic moduli of olivine (e.g., Jacobsen et al., 2008). As expected, V_s decreases with increasing temperature because of decreasing shear modulus.

2.2 Electrical conductivity and water content

The mantle minerals (i.e., olivine, pyroxene, and garnet) are nominally anhydrous but can contain small amounts of water (up to a few hundreds or thousands of ppm H/Si), which can have a significant effect on the electrical conductivity because diffusing hydrogen can carry charge. The magnitude of this effect on conductivity differs from different studies (e.g., Gardés et al., 2014; Wang et al., 2006; Yoshino et al., 2009) so we utilize the unified hydrous conductivity model of Gardés et al. (2014) in calculating the total electrical conductivity (violet lines) of olivine as a function of C_{OH} and T (Fig. 1b). From this, the C_{OH} for a region can be constrained if electrical conductivity is known as well as its seismically-inferred temperature range (section 2.1).

2.3 Effective viscosity: estimation and sensitivity to controlling parameters

The deformation mechanism map (Fig. 1c), with its associated effective viscosity contour lines (dotted grey lines) can be used to (i) estimate the effective viscosity range bounded by the inferred T (section 2.1) and C_{OH} (section 2.2) ranges, and (ii) investigate how effective viscosity varies with C_{OH} and T for different dominant deformation mechanisms. Each deformation mechanism varies differently with stress and grain size (Table 1), with diffusion creep highly sensitive to grain size, dislocation creep highly sensitive to stress, and DisGBS sensitive to both parameters, as explored in more detail in Section 4. DisGBS, which is not present in Fig. 1c, becomes dominant at dry conditions under weak stresses (Section 4). Notably, moving from wet to dry conditions

(Fig. 1c) results in > 1 order of magnitude increase in effective viscosity. This highlights the importance of constraining water content when estimating viscosity.

Table 1. Parameters Used in Viscosity Calculations. All the parameters for dislocation and diffusion creep are taken from Hirth and Kohlstedt (2003), while dislocation-accommodated grain-boundary sliding (DisGBS) values are from Ohuchi et al. (2015). We use water fugacity f_{H2O} values in calculating strain rate by converting C_{OH} to f_{H2O} using Zhao et al. (2004). We multiply wet dislocation and diffusion strain rates by a factor of 3.5^r to account for Bell et al. (2003) calibration, which is accounted for by Zhao et al. (2004) but not by Hirth and Kohlstedt (2003).

Deformation	A ($m^p s^{-1} MPa^{-n-r}$)	n	p	r	E* (kJ/mol)	V* (cm^3/mol)
Dry dislocation	1.1×10^5	3.5	-	-	530	15
Wet dislocation	1.6×10^3	3.5	-	1.2	520	22
Dry diffusion	1.5×10^{-9}	1	3	-	375	6
Wet diffusion	2.5×10^{-11}	1	3	1	375	14
DisGBS	1.288×10^{-5}	3	1	1.25	423	17.6

3 Viscosity estimates from geophysical measurements

Because some uncertainty is associated with every geophysical observation, our estimates of viscosity from seismic (section 3.1), MT (section 3.2), and both seismic and MT (section 3.3) must also include an estimate of uncertainty, resulting in a viscosity range. For all cases, we visualize the possible viscosities for a region as a grey patch (Fig. 2) within the constructed deformation mechanism map. Using this patch, we determine the range of the logarithm of the effective viscosity ($log\,\bar{\eta} \pm log\,\Delta\eta$), where log of average effective viscosity ($log\,\bar{\eta}$) and log of viscosity uncertainty ($log\,\Delta\eta$) are calculated by:

$$log\,\bar{\eta} = \frac{(log\eta_{max} + log\eta_{min})}{2} \quad (3.1)$$

$$log\,\Delta\eta = \frac{(log\eta_{max} - log\eta_{min})}{2} \quad (3.2)$$

where η_{max} and η_{min} are the maximum and minimum effective viscosities found within the patch, respectively. We determine the effective viscosity range for dry and wet upper mantle separately, to determine which viscosity law controls the overall viscosity range.

In this theoretical investigation, the geophysical uncertainties that we set for seismics and MT are arbitrary but approximately align with common model uncertainties. For actual geophysical observations, uncertainties depend on the Earth structure, composition and data quality. For seismics, we assume an uncertainty of ± 0.05 km/s, which is the average V_s uncertainty from phase velocities at the 50 – 150 s period range that is sensitive to V_s structure in the lithospheric mantle and asthenosphere (Lebedev, Boonen, & Trampert, 2009). We assume an electrical conductivity uncertainty of ± 0.5 log S/m, which we estimate based on the inferred conductivity ranges in Selway et al. (2019).

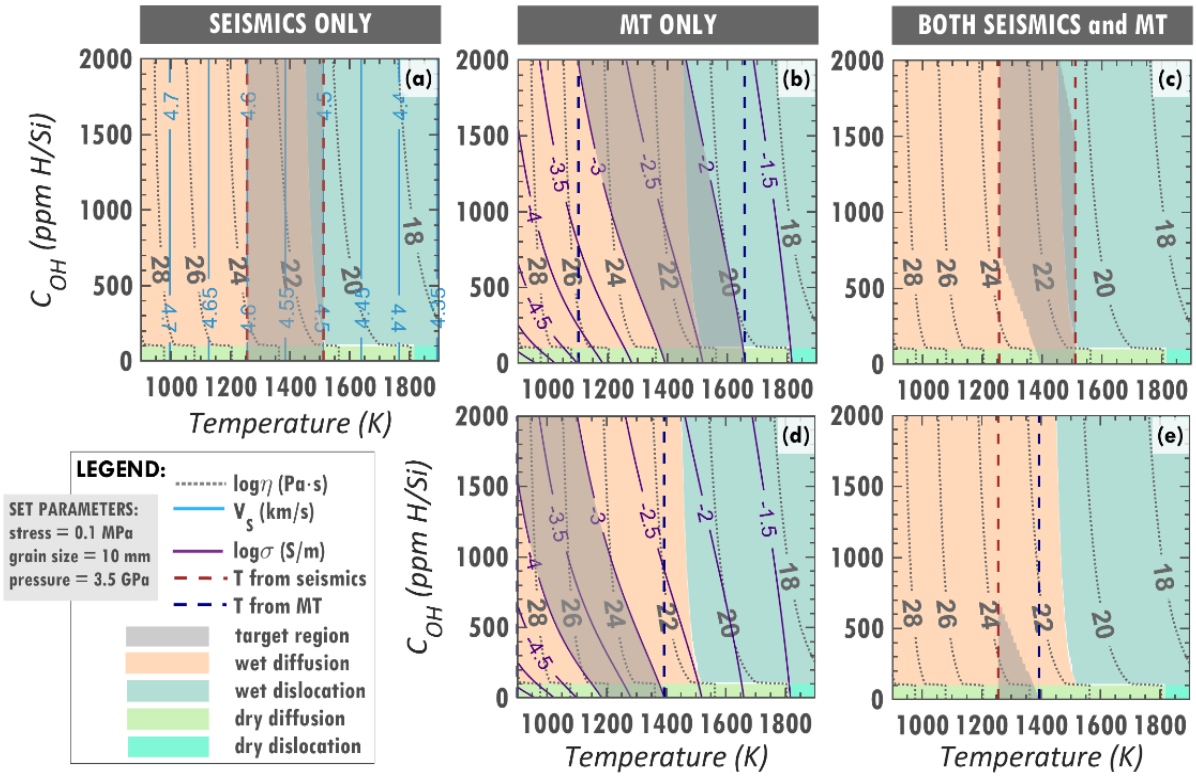

Figure 2. Estimating viscosity from (a) seismic, (b,d) MT, and (c,e) both seismic and MT constraints. The effective viscosity range for a target region with assumed geophysical observation/s (with uncertainty) is described by the minimum and maximum viscosities that fall within the grey patch. The region has an assumed $V_S = (4.55 \pm 0.05) km/s$ and $\sigma = (2.5 \pm 0.5)\ log\ S/m$ or $(3.5 \pm 0.5)\ log\ S/m$. When considering only the (a) V_S or the (b,d) σ constraints, the grey patch is relatively wide, covering a large viscosity range. This viscosity range is reduced (with smaller grey patches in (c) and (e)) when both MT and seismic constraints are considered. Better constraints on viscosity are possible if there is a small overlap between seismic and MT curves (as in e).

3.1 Absolute seismic velocity models only

As an example, we assume a melt-free region with an olivine grain size of 10 mm at 3.5 GPa pressure (~115 km depth) under a weak stress of 0.1 MPa. Initially, we assume that only seismic data are available and that the modelled shear wave velocity is (4.55 ± 0.05) km/s. Using the deformation mechanism map with V_S contour lines (Fig. 2a), the given V_S range converts to a temperature range (red dashed lines). Since water content is not constrained by seismic data, the grey patch has the full (0 to 2000 ppm H/Si) water content range resulting in a relatively large possible viscosity range, where diffusion creep is the dominant deformation mechanism for dry ($\leq$100 ppm H/Si) and partly diffusion and dislocation for wet (>100 ppm H/Si) conditions. The estimated overall viscosity range as well as the separate dry and wet viscosity ranges (F2a in Fig. 3a) are summarized in Table 2. As expected, the dry olivine is more viscous than the wet olivine. Its associated uncertainty (Fig. 3b) is smaller because of the smaller water content range. The overall viscosity has a large uncertainty of 2.5 orders of magnitude due to the unconstrained water content and the assumed V_S uncertainty.

We perform the same process to determine dry, wet and overall viscosity ranges (Fig. 3a and 3b) for regions with different V_S but the same pressure, stress, grain size and V_S uncertainty. For

increasing V_S (decreasing temperature), the corresponding dry, wet and overall viscosities increase both in magnitude and uncertainty. However, dry viscosity uncertainties become greater than those for wet viscosities for $V_S \geq (4.60 \pm 0.5)$ km/s because the dry viscosity varies significantly across inferred low temperatures. Consistently, the calculated viscosity uncertainties are mostly greater than one order of magnitude, which indicates relatively large viscosity ranges for regions with seismic constraints only.

3.2 Electrical conductivity models only

Now, we consider that the same region is instead observed using MT only, and viscosity is inferred from electrical conductivity (e.g., $10^{-(2.5\pm0.5)}$ S/m and $10^{-(3.5\pm0.5)}$ S/m in Fig. 2b and 2d, respectively). Estimates of viscosity as a function of conductivity are depicted in Fig. 3c for both dry and wet viscosity assumptions. If the region is more conductive (F2b in Fig. 3c), the viscosity uncertainty (Fig. 3d) is smaller compared to a less conductive case (F2d) because of the thermal effects on viscosity and conductivity (contours in Fig. 2b). Consistently, the less conductive regions are more viscous and generally have larger viscosity uncertainties. Notably, the overall

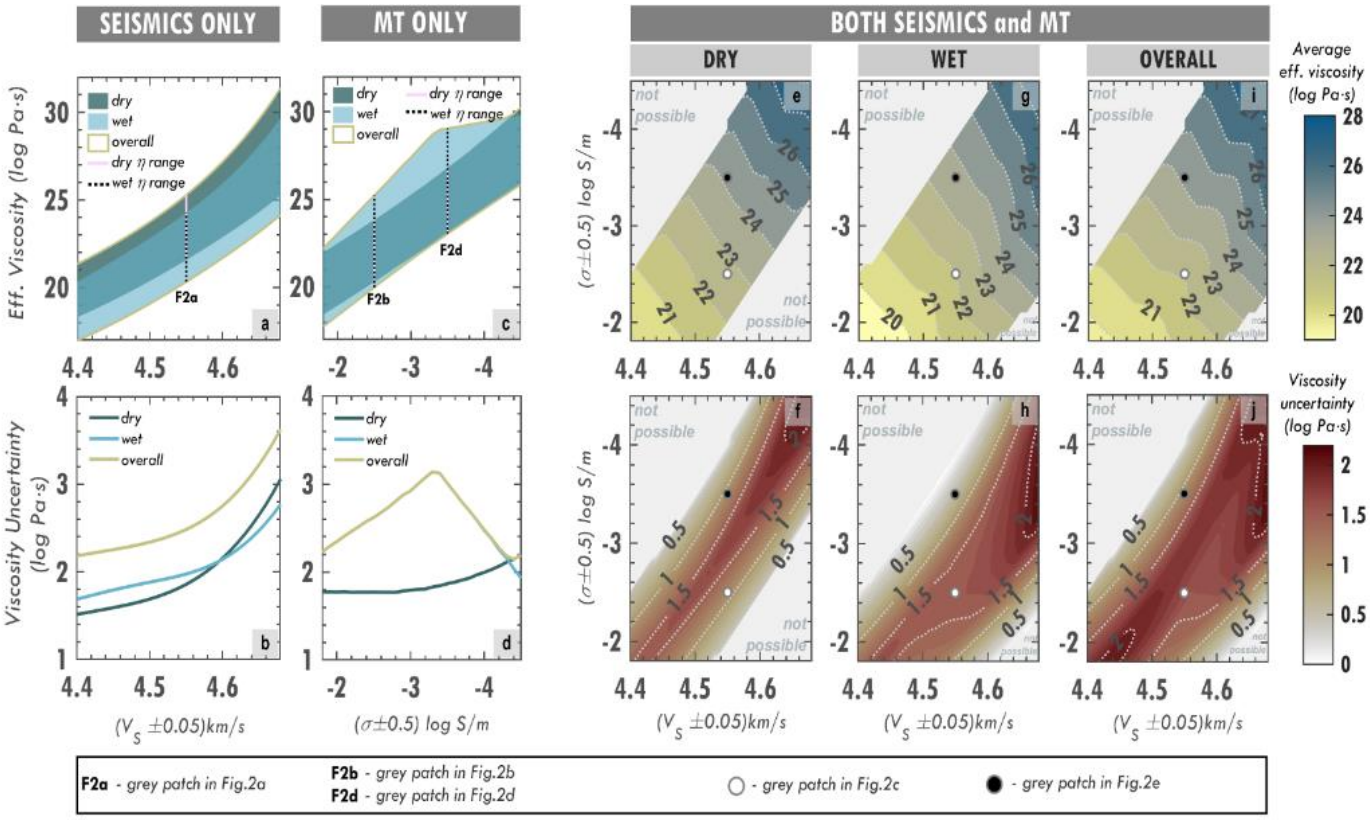

Figure 3. Viscosity estimates from geophysical observations. The effective viscosities are calculated for 10 mm olivine grain size at 3.5 GPa under 0.1 MPa stress (as in Fig. 2). Dry (≤ 100 ppm H/Si), wet (> 100 ppm H/Si) and overall viscosities are estimated based on constraints from different geophysical observations. The black dotted and pink solid lines (a,c), and the black and white dots (e-j) indicate the viscosity estimates for the sample regions in Figure 2. When both seismics and MT are considered (e-j), viscosity uncertainties are relatively low compared to either seismics or MT alone (a-d). This uncertainty decreases as the overlap in velocity and conductivity constraints decreases (e.g., Fig. 2e) until the two constraints become incompatible ('not possible' portions in e-j panels).

viscosities can generally be estimated from the wet viscosities, indicating that the wet viscosity laws control the overall estimates. The overall viscosity uncertainties are smaller than those with seismics only constraints. The turning point at approximately $-(3.4 \pm 0.5)$ log S/m is due to the imposed minimum temperature bound of 900 K which forces regions with lower conductivities to have lower water contents (left side of Fig. 2d). The viscosity uncertainties are mostly greater than 1.5 order of magnitude, which indicates relatively large viscosity ranges for the regions with MT constraints only.

Table 2. Viscosity estimates from geophysical constraints using different stress-grain size combinations or ranges. In this example we have assumed $V_s = (4.55 \pm 0.05)$ km/s and $\sigma = -(2.5 \pm 0.5)$ log S/m as in Fig. 2(a-c).
[a] mantle convection-induced stress/es
[b] glaciation/deglaciation-induced stresses
[c] The value encompasses both dry and wet conditions, which provides the overall viscosity, or just one of these two conditions depending on the constrained water content. Its calculated viscosity range may be the same as that of the wet or dry condition, which may indicate that (i) the region is entirely wet or entirely dry or (ii) the wet and dry viscosity ranges are coincident as in Fig. 3c.

Stress (MPa)	**Grain size (mm)**	**Condition**	**Effective viscosity ($Pa \cdot s$)**		
			Seismics Only	*MT Only*	*Both Seismics and MT*
0.1 [a]	10	Dry	23.1 ± 1.9	21.8 ± 1.8	22.4 ± 1.1
		Wet	22.0 ± 2.0	22.3 ± 2.6	21.7 ± 1.6
		Overall [c]	22.5 ± 2.5	22.3 ± 2.6	21.9 ± 1.7
$0.1 - 8$ [a]	1 – 10	Dry	20.9 ± 4.1	19.4 ± 4.1	20.2 ± 3.4
		Wet	19.7 ± 4.3	20.0 ± 4.9	19.5 ± 3.8
		Overall [c]	20.2 ± 4.8	20.0 ± 4.9	19.6 ± 4.0
$5 - 30$ [b]	1 – 10	Dry	19.3 ± 3.9	17.4 ± 3.5	18.2 ± 2.8
		Wet	17.4 ± 3.4	18.0 ± 4.4	17.1 ± 2.9
		Overall [c]	18.6 ± 4.5	18.0 ± 4.4	17.6 ± 3.4

3.3 Both seismic and electrical conductivity models

Next, we assume that the region has both seismic and MT measurements (Fig. 2c and 2e). We use the seismically-determined temperature range to constrain the water content range from the electrical conductivity curve. Visually, we can simply overlay the grey patches in 'Seismics Only' and 'MT Only' cases. This overlap results in the grey patch for 'Both seismics and MT' case which is smaller than the patches in the former cases. Consequently, their dry, wet and overall viscosities have reduced viscosity uncertainties (white and black dots in Fig. 3e-3j). When one geophysical observation (either MT or seismics) estimates lower temperatures (e.g., Fig. 2a dry) and the other observation estimates higher temperatures (Fig. 2b dry), the combined patch is for intermediate temperatures (Fig. 2c dry). However, when the patches from both MT and seismics indicate similar temperatures or one patch lies within the other patch, the use of both constraints may not significantly improve the viscosity uncertainty (e.g., white dot in Fig. 3h). In contrast, we can

obtain better constraints on viscosity (black dots in Fig. 3) for regions where electrical conductivity and seismic curves do not overlap much, and in this case MT improves the temperature estimates.

4 Complexities from stress and grain size

Here we investigate how changing the stress and grain size affects the viscosity and the associated uncertainty for the region of interest. In this study, we consider 1-10 mm grain sizes (e.g., Ave Lallemant et al., 1980) and lithospheric stresses of 0.1 – 100 MPa (Fig. 4), where stresses ≤ 8 MPa are typically associated with mantle convection (Conrad & Lithgow-Bertelloni, 2006) and stresses ≤ 30 MPa are associated with glaciation (e.g., Johnston et al., 1998).

4.1 Large stresses and big grain sizes: Dislocation creep domain

The inferred effective viscosity and the associated uncertainties for a melt-free region under large stresses (> 10 MPa, Fig. 4) do not vary significantly with grain size. For these large stresses, the dominant deformation mechanism is dislocation creep, which is grain size independent but strongly stress dependent. This dislocation creep domain extends down to relatively weak stresses (≤ 1 MPa) but only for olivine grain sizes of at least 3 mm, depending whether the region is dry (Fig. 4a) or wet (Fig. 4b).

4.2 Weak stresses and small grain sizes: Diffusion creep domain

For weak stresses (≤ 1 MPa, Fig. 4), the average effective viscosities and the associated uncertainties vary with grain size and diffusion creep is the most important mechanism across 1 – 10 mm grain sizes. Within the diffusion creep domain, the average effective viscosity does not change with stress but is instead sensitive to grain size. The inferred viscosity uncertainties for weak stresses in the diffusion creep domain are smaller than those for stresses in the dislocation creep domain. This emphasizes the importance of the deformation mechanism, which is controlled by stress and grain size, when estimating viscosity and its uncertainty.

4.3 Intermediate stresses: Transition between diffusion and dislocation domains

For intermediate grain sizes and stresses, multiple deformation mechanisms may function together (brown, grey and stone blue regions, Fig. 4) which we describe here as transition regimes. These transition regimes are defined as those where the grey patches calculated from the geophysical responses (Fig. 2) overlie more than one dominant deformation mechanism. Consequently, the average viscosities and uncertainties become sensitive to both stress and grain size and vary more rapidly than when one regime dominates, particularly in wet conditions (brown regions, Fig. 4b). For the dry 'Seismics Only' case, DisGBS also contributes to deformation at intermediate stresses (1-10 MPa).

4.4 Viscosity estimates using stress and grain size ranges

Since stress and grain size are often unknown, we must consider a range for these parameters within Figure 4. Clearly, considering ranges for stress and grain size increases the viscosity uncertainty compared to just considering a single choice (as in Fig. 2). This increase in viscosity uncertainty is greatly affected by the deformation mechanism(s) functioning in the region of

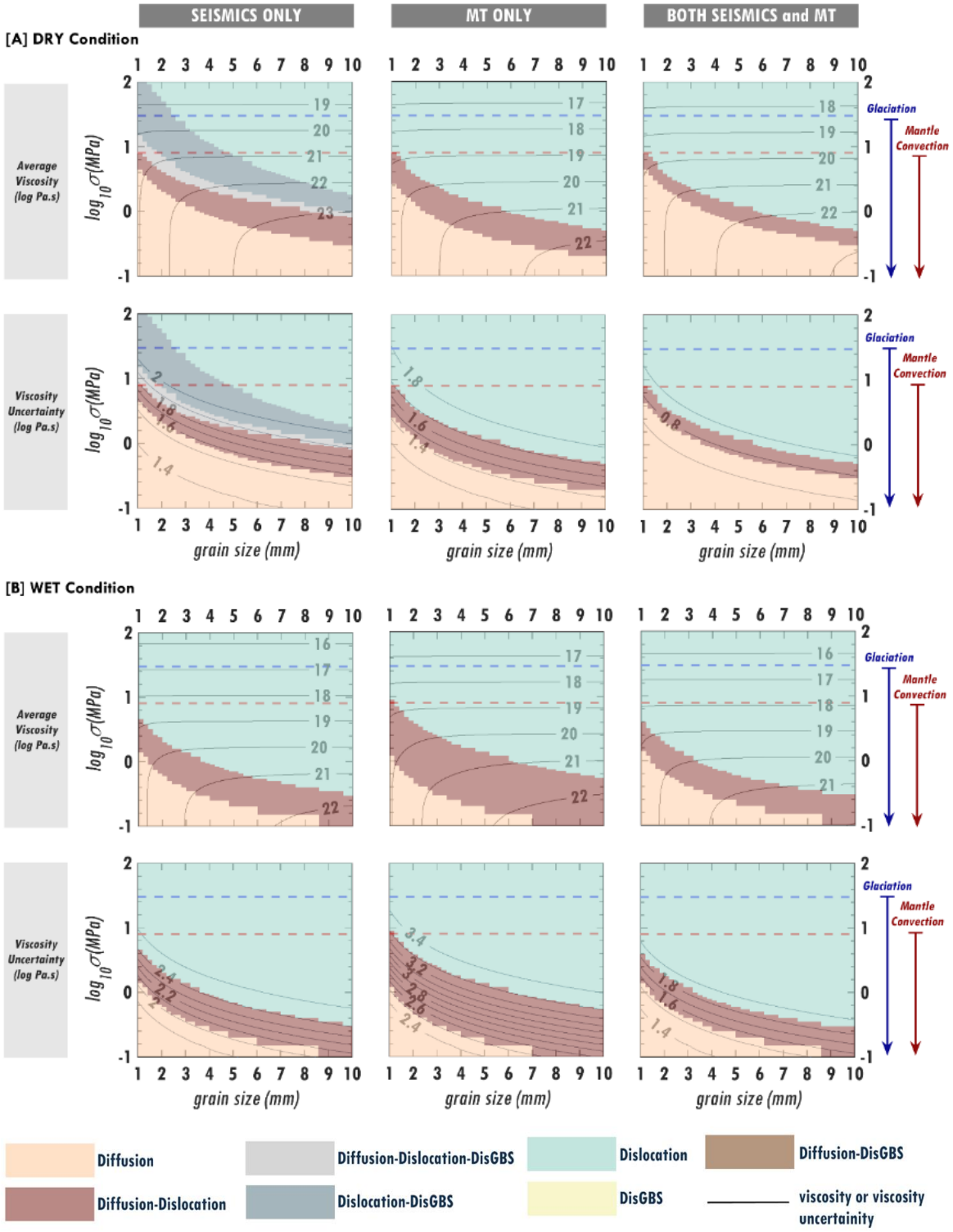

Figure 4. Viscosity estimates across stress and grain size space for [A] dry and [B] wet conditions. Shown are viscosity ranges (average viscosities and uncertainties) for a region with the same assumed geophysical constraint/s as in Figure 2(a-c), calculated for different stress and grain size combinations. The dominant deformation mechanisms are plotted as colored regions (legend), and indicate controls on viscosity and its dependence on stress and grain size (primary controllers for deformation mechanism).

306 interest. The dry and wet upper mantle under mantle convection stresses (0.1 – 8 MPa) over 1-10

mm grain sizes in Fig. 4 have more combinations of possible deformation mechanisms than those under higher, glaciation-induced stresses (8-30 MPa). Notably, this complexity results in relatively large viscosity uncertainties for mantle convection stresses (Table 2), where viscosity is strongly controlled by both stress (dislocation creep and DisGBS) and grain size (diffusion creep and DisGBS).

5 The effect of bulk composition on geophysical constraints

We expect heterogeneity in bulk composition of the upper mantle, and this is important because different rock compositions have different electrical conductivities and seismic velocities affected by variability in silica, iron and calcium content, and modal mineralogy (e.g., Xu et al., 2008; Karato & Karki, 2001). Thus, seismic velocity variations, often attributed solely to temperature variations, may also be due to variations in rock composition. This affects our interpretation of observed variations in seismic velocity and adds additional uncertainty when converting seismic velocity into temperature and viscosity. In addition, different minerals in mantle rock have different conductivities, and bulk conductivity is also affected by water content of different minerals, water partitioning between the minerals and interconnectivity of the different phases (e.g., Özaydin & Selway, 2020), which adds additional uncertainty into our viscosity calculations.

5.1 Seismic velocities for different compositions and geotherms

Using the bulk compositions for pyrolite and harzburgite in Xu et al. (2008), we compute the stable phase assemblages at given pressure-temperature (P-T) conditions (Fig. 5) as well as the corresponding seismic velocities (Fig. 6a) using the self-consistent thermodynamic formalism (HeFESTo) of Stixrude and Lithgow-Bertelloni (2005b, 2011) for each of the geotherms (Fig. 6c). The modelled V_S are corrected for dispersion using the seismic attenuation model QR19 (Romanowicz, 1995), where attenuation is strongest at shallower upper mantle depths (100 – 250 km) and then decreases at greater depths. Attenuation affects measured seismic wave speeds and will therefore impact our viscosity interpretations. Attenuation is often challenging to measure directly (e.g., Dalton & Ekström, 2006a; Dalton et al., 2008) but is intrinsically linked to viscosity because deformation processes at the grain scale will also anelastically absorb seismic energy. We consider pyrolite and harzburgite here because they are geologically common and have distinct physical properties at the same pressure and temperature conditions (Fig. 6a). We construct models (Fig. 6c) for the geotherm based on a cold cratonic environment (blue line) and a warmer plume-influenced environment (red line). Each geotherm grades from a surface temperature of $T_0 = 0℃$ to a mantle adiabat at the base of the lithosphere at 150 km and 80 km depth for the cratonic and plume-influenced environments, respectively (details in Appendix). The cratonic mantle potential temperature is 1623 K and the adiabat is 0.4 K/km and the plume-influenced geotherm is assumed to have an excess mantle potential temperature of approximately 100 K with respect to the cratonic geotherm, which agrees with the observations for many plumes (e.g., Courtier et al. 2007). The

parameters in all models are chosen based on common geophysical observations such as surface heat flux.

Phase proportions vary significantly with bulk composition, and less with temperature, except at shallow depths (Fig. 5a). The difference in olivine, garnet and orthopyroxene modal mineralogy between harzburgite and pyrolite at the same geotherm results in a seismic velocity difference of $\sim 0.02 - 0.05$ km/s below 150 km depth (Fig. 6a). For the same composition but different geotherm, a seismic velocity variation of $\sim 0.05 - 0.10$ km/s is mainly due to the thermal difference ($\sim$100 K), not from the minimal change in garnet and orthopyroxene proportions (e.g., Fig. 5a & c). Moreover, the LVZ for the plume-influenced environment occurs at shallower depths with lower minimum velocity than for the cratonic environment. In our modelled scenarios, the phase transition from olivine to wadsleyite occurs at slightly different depths and with different V_S ranges due to the combined effects of temperature and composition. Clearly, seismic velocity is

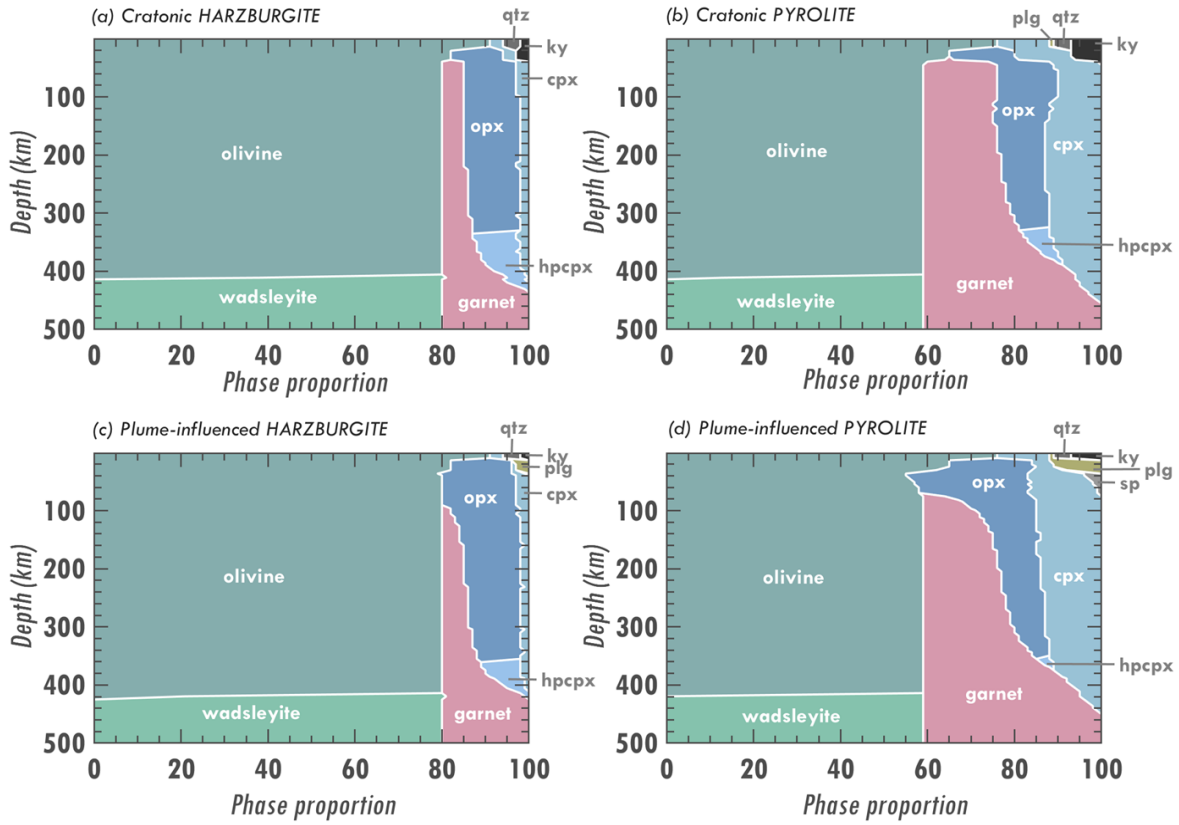

Figure 5. Phase proportions of (a,c) harzburgite and (b,d) pyrolite with (a,b) cratonic (colder, Fig. 6c) and (c,d) plume-influenced (hotter, Fig. 6c) geotherms. Phases are: plagioclase (plg), spinel (sp), quartz (qtz), kyanite (ky), orthopyroxne (opx), clinopyroxene (cpx), high-pressure Mg-rich clinopyroxene (hpcpx), garnet (gt), olivine (ol) and wadsleyite (wa). Computed with HeFESTo (Stixrude & Lithgow-Bertelloni 2011) using the bulk compositions from Xu et al. (2008).

dependent on both temperature and composition, and variations in both of these parameters result in seismic velocity anomalies.

5.2 Electrical conductivities for different compositions and geotherms

The bulk conductivity of a mantle rock is controlled by its modal mineralogy, bulk water content, water partitioning, interconnectivity and conductivity of the individual phases. To see how the bulk conductivity varies for different compositions, we forward model the overall conductivities for harzburgite and pyrolite using the MATE software (Özaydin & Selway, 2020). We use the geotherms in Fig. 6c and modal mineralogy in Fig. 5. We use a modified Archie's law to define

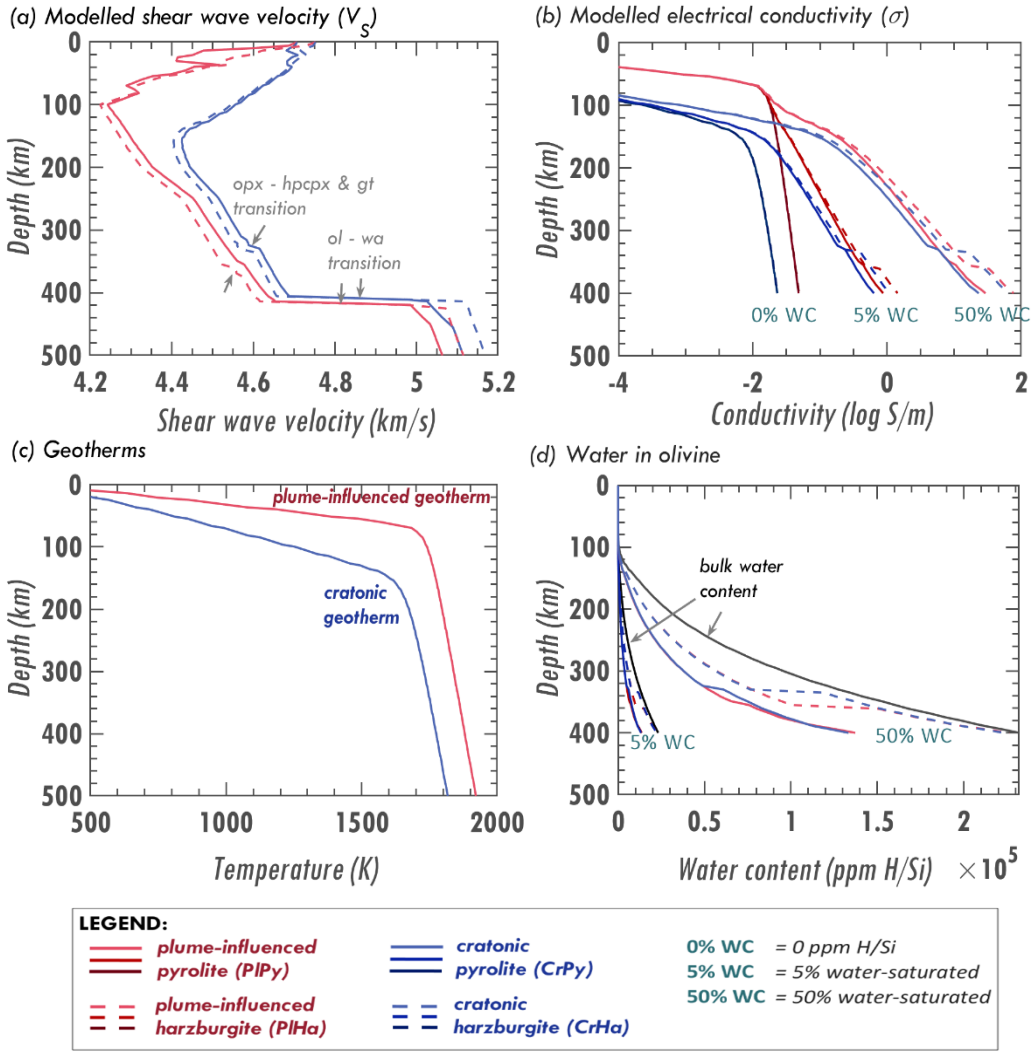

Figure 6. Modelled (a) shear wave velocities V_S and (b) electrical conductivities σ for pyrolite (solid lines) and harzburgite (dashed lines) for (c) cratonic (blue lines) and plume-influenced (red lines) geotherms. (a) The V_S trends of the compositions in Figure 5 are calculated using HeFESTo (Stixrude & Lithgow-Bertelloni 2005b), and are corrected for attenuation. The grey arrows indicate phase transitions (see Figure 5). (b) The forward modelled bulk σ for compositions in Figure 5 at different bulk water content: 0 ppm H/Si (darkest lines), 5% water saturation (medium lines) and 50% water saturation (palest lines) using MATE software. Water saturation of the rock is quantified as the water solubility of olivine based on the Padrón-Navarta and Hermann (2017) formulation. (d) MATE calculation of water in olivine (blue and red lines) for different compositions and geotherms from the given bulk water content (5%, black line or 50%, grey line) based on the used partitioning coefficients.

the rock geometry and assume that olivine is perfectly connected (m=1), abundant pyroxene (10-15%) is well connected (m=2) and other minerals are very poorly connected (m=4), where m is the Archie's law connection exponent (Glover, 2010). We assume different bulk water content to see how it affects both the electrical conductivity (Fig. 6c) and the viscosity estimates from MT constraints for pyrolite and harzburgite (Section 6). We consider three conditions: completely dry (0% WC), 5% water-saturated (5% WC), and 50% water-saturated (50% WC) mantle rocks. We define water saturation from the subsolidus olivine water solubility formulation of Padrón-Navarta & Hermann (2017) because we assume a melt-free mantle and the bulk of the experimental data relate to olivine.

The composition with higher bulk water content (50% WC) is significantly more conductive than the 5% WC or 0% WC compositions (Fig. 6b). For each bulk water content, the composition with plume-influenced (hotter) geotherm is consistently more conductive than cratonic (colder) composition. These indicate the sensitivity of conductivity to both water and temperature. In contrast, modal mineralogy has a smaller impact on the overall conductivity as seen from the minimal conductivity difference between harzburgite (dashed lines) and pyrolite (solid lines) but becomes more significant when more water is involved. Since bulk water in a mantle rock is partitioned across the constituent phases based on their individual partition coefficients, the water contents of individual minerals may change for different compositions at different bulk water contents. Consistently, olivine in harzburgite contains more water than olivine in pyrolite (Fig. 6d) because more water in pyrolite has been partitioned to the pyroxene phases. Because of this extra water, we expect harzburgite to be less viscous than pyrolite for the same geotherm.

5.3 Effect of composition on viscosity estimates from seismic velocity models

We forward modelled dry and wet viscosity structures (Fig. 7) from modelled V_S profiles of the cratonic harzburgite and plume-influenced pyrolite using the method described in Section 3.1. As before, we add a constant velocity uncertainty of ± 0.05 km/s for each V_S profile (Fig. 7a) and calculate the temperatures for each composition (Fig. 7b), assuming that the uncertainty for V_S is associated with uncertainties in temperature. The inferred temperatures are used in the viscosity calculation for both dry (≤ 100 ppm H/Si) and wet (> 100 ppm H/Si) conditions.

The uncertainty in the interpreted thermal structure is smaller at depths shallower than ~ 250 km than at greater depths, which results in more tightly constrained dry (Fig. 7c) and wet (Fig. 7d) viscosity structures. This implies that attenuation, which is stronger at shallower upper mantle depths, clearly influences viscosity estimates.

Compositional and thermal effects on seismic velocities may offset each other. In our models, this results in partially overlapping seismic velocities of colder cratonic harzburgite and hotter plume-influenced pyrolite at depths below ~200 km (Fig. 7a). However, because we interpret these models with their known compositions, the inferred thermal and viscosity structures of the two models are different. If we were to assume that seismic velocity is dominantly temperature dependent, we would interpret that the velocity overlap at these depths implies that the regions have the same temperature and viscosity. This erroneous interpretation highlights the limitation of

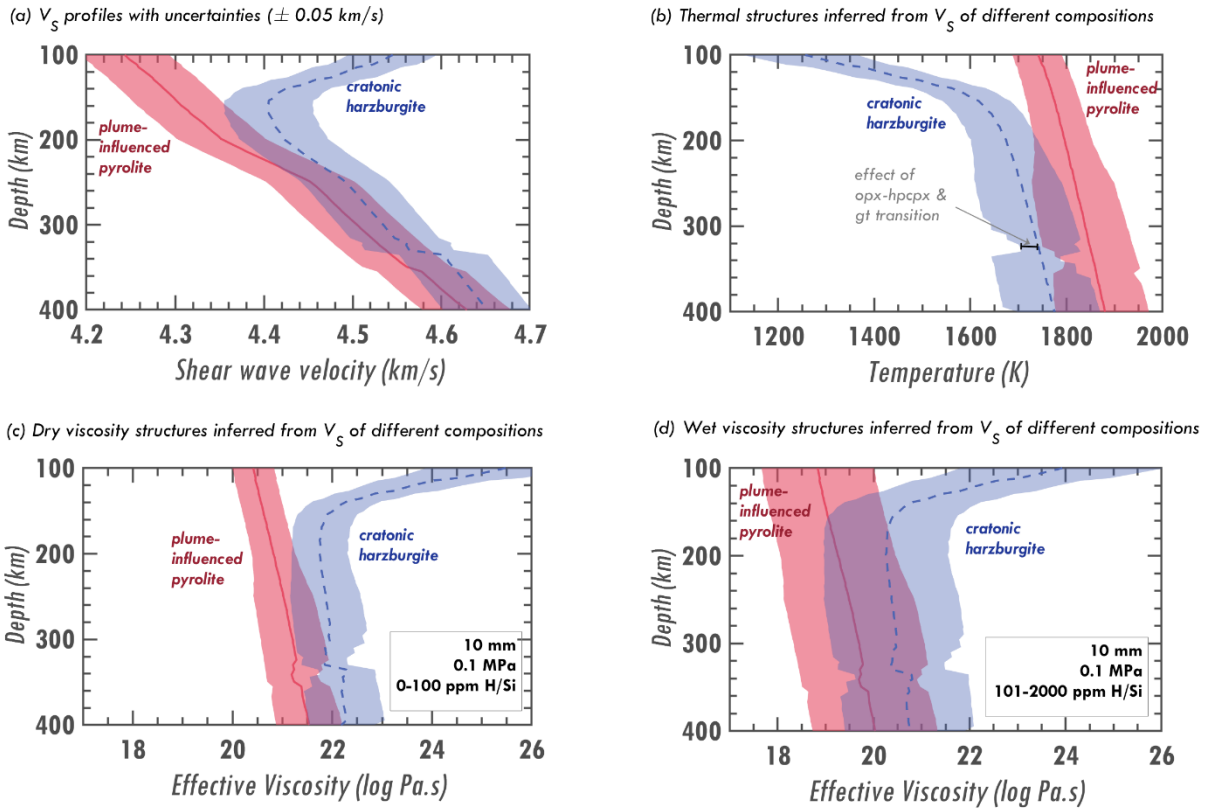

Figure 7. Constructing viscosity structures from shear wave velocities. (a) Shear wave velocity structures with constant uncertainty for plume-influenced pyrolite (pink band) and cratonic harzburgite (blue band). Partial overlap of both velocity structures occurs due to the applied velocity uncertainty. **(b)** The thermal structures inferred from the V_S structures in (a). At depths where kinks are present, the lower bound temperatures of pyrolite and harzburgite increase and become closer to the average temperatures (black segment) because of the phase transitions (opx-hpcpx and opx-gt) that occur at these temperatures and depths. **(c)** Dry and **(d)** wet viscosities calculated using the method of Section 3.1, which mainly uses seismically-inferred temperatures in (b) and unconstrained water content ranges for dry (≤100 ppm H/Si) and wet (>100 ppm H/Si) conditions. Note that the observed velocity overlaps do not correspond perfectly to the thermal and viscosity overlaps.

this assumption and demonstrates that we need to account for compositional variations when inferring thermal and viscous properties from seismic data.

For most depths, the plume-influenced pyrolite has a larger temperature range than the cratonic harzburgite. At depths where we observe large portion of overlapping V_S, there are kinks on the lower temperature bounds for both harzburgite and pyrolite caused by phase transitions (orthopyroxene to garnet (opx-gt) and orthopyroxene to high pressure magnesium-rich clinopyroxene (opx-hpcpx), Fig. 5 and 6a). At these phase transitions, seismic velocity changes significantly with a small change in temperature, which reduces the uncertainty in temperature. Thus, the phase transition also affects the viscosity estimates.

6 Testing the method

We forward model synthetic viscosity structures (Fig. 8a-c) for the chosen harzburgite and pyrolite compositions (Fig. 5), geotherms (Fig. 6c), water contents (Fig. 6d), stresses and grain sizes. Then, we attempt to reconstruct these synthetic viscosity structures from computed geophysical

observations (with uncertainty) that we would expect from these structures (Fig. 9a-c). These tests are designed to demonstrate the utility of our developed method and assess its precision (Fig. 9d-e) and accuracy (Fig. 9f-g). In doing so, we highlight the impact of composition, water content, geophysical observations and geophysical uncertainties when constraining viscosity estimates.

6.1 Forward modelled synthetic viscosities

The modelled temperature, water content, stress, grain size and composition (particularly olivine proportion) heterogeneities in the upper mantle result in variations in viscosity (Fig. 8). We consider different geotherms (cratonic and plume-influenced), water concentrations set to 0%, 5% and 50% of water saturated conditions, stresses (0.1 and 1 MPa), grain sizes (4 and 10 mm), and compositions (harzburgite *Ha* and pyrolite *Py*) (Fig. 8a-c). At depths below 200 km, we identify the dominant deformation mechanism. The diffusion creep mechanism, which is dominant at small stresses, leads to increasing viscosity with depth for dry conditions because it is sensitive to increasing pressure. However, in wet conditions, diffusion creep leads to decreasing viscosity with depth due to its water sensitivity and because, in our compositions defined as 5% and 50% water

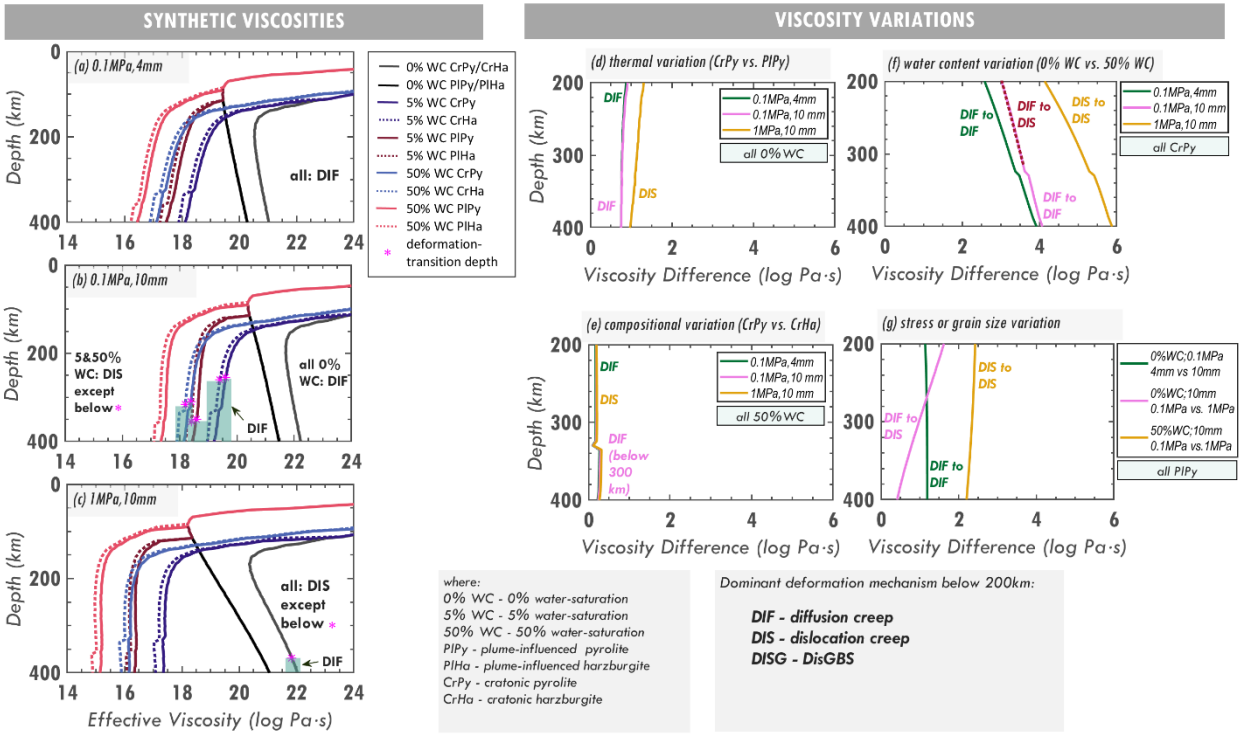

Figure 8. (a-c) Synthetic viscosities and (d-g) viscosity variations for harzburgite and pyrolite at different geotherms, water concentrations, stresses and grain sizes. These viscosities are calculated using the geotherms and water concentrations in Fig. 6c and d, respectively. For each panel in (a-c), three groups of viscosity structures can be identified based on their bulk water concentration: 0% WC, 5% WC and 50% WC, where viscosities for 0% WC do not depend on composition (CrPy/CrHa and PlPy/PlHa pairs overlap). The dominant deformation mechanism below 200 km is included (see legend), where the synthetic viscosity structures in the same group (same bulk water) have the same deformation mechanism. All viscosities are produced by (a) diffusion creep at small stress and grain size, (b) varying mechanisms at small stress and large grain size, and (c) dislocation creep at relatively large stress & grain size. Differences between pairs of viscosity curves (d to g) show the relative effects of (d) thermal, (e) compositional, (f) water content, and (g) stress and grain size variations on viscosity. Mostly in panels (d) to (g), the dislocation regime produces the largest viscosity variation (in magnitude).

saturated, water content increases with depth. In contrast, dislocation creep yields an approximately constant viscosity with depth for wet conditions because of the counter-balancing effects from pressure and water. This behavior is not evident in dry conditions, where viscosity increases significantly with depth due to the strong sensitivity of dislocation creep to pressure (Table 1).

Interestingly, for dry conditions (Fig. 8a-c, 0%WC) our calculations produce a low viscosity layer at the top of the asthenosphere without introducing composition or grain size variations across the lithosphere-asthenosphere boundary (LAB). Based on geophysical observations and experiments, this low viscosity layer, which may help to stabilize plate tectonics (e.g., Richards et al., 2001), has been attributed to partial melt (e.g., Chantel et al., 2016; Selway & O'Donnell, 2019) or to solid-state mechanisms (e.g. Faul & Jackson, 2005) or to hydrogen content (Karato, 2012). Changes in composition such as these have not been tested in our models but our results show that for dehydrated upper mantle, the upper asthenosphere could have a low viscosity without needing to invoke compositional changes (e.g., Karato, 2010).

A 100 K temperature difference can produce about an order of magnitude viscosity variation (Fig. 8d), while the presence of water (i.e., from 0% to 50% water saturation) can result in a larger change in viscosity (2-6 orders of magnitude, Fig. 8f) that clearly emphasizes the need to constrain water in the upper mantle. Change in stress and/or grain size produces ~0.5-2 orders of magnitude change in viscosity (Fig. 8g). A compositional change from pyrolite to harzburgite varies the viscosity by a factor of two (Fig. 8e), which is measurable but not as big as the other factors. Nonetheless, compositional variations clearly affect the seismic velocity and conductivity observations and the temperature and water content parameters that are inferred from them. Apart from these factors, the dominant deformation mechanism can also impact the magnitude of the viscosity change, where the dislocation creep regime results in a larger viscosity variation compared to the diffusion creep regime (Fig. 8d-g).

6.2 Reconstructed viscosities from geophysical observations

Commonly, we cannot constrain the composition of the upper mantle using geophysical observations, but instead must refer to petrological studies. We also do not know the true geotherm. Many studies (e.g., Goes et al., 2000; Heezsel et al., 2016; Milne et al., 2018; Lucas et al., 2020) construct the thermal structure using seismics without accounting for variations in composition that could affect seismic velocities and therefore temperature and viscosity estimates. To investigate how compositional variations may impact viscosity estimates, we assume two known upper mantle compositions (harzburgite and pyrolite) in a cratonic setting. We reconstruct their synthetic viscosity structures at 0.1 MPa stress and 10 mm grain size using our developed method where their modelled seismic velocities (Fig. 6a) and electrical conductivities (Fig. 6b) are converted into temperatures and water concentrations, respectively (Fig. 9a-c). We consider the modelled electrical conductivities for 0%, 5% and 50% of water saturation and infer these water concentrations and their associated uncertainties via MATE software. Figure 9(a-c) shows the reconstructed viscosities that would be calculated if only seismic or if both seismic and MT data were available, in comparison with the forward modelled synthetic viscosities. We consider different geophysical uncertainties ([0.05 km/s, 0.5 log S/m] and [0.03 km/s, 0.3 log S/m]) to assess their effect on viscosity estimates. From these assumptions, we evaluate the developed method by quantifying how well both MT and seismics can constrain viscosity estimates (Fig. 9d-e), and by

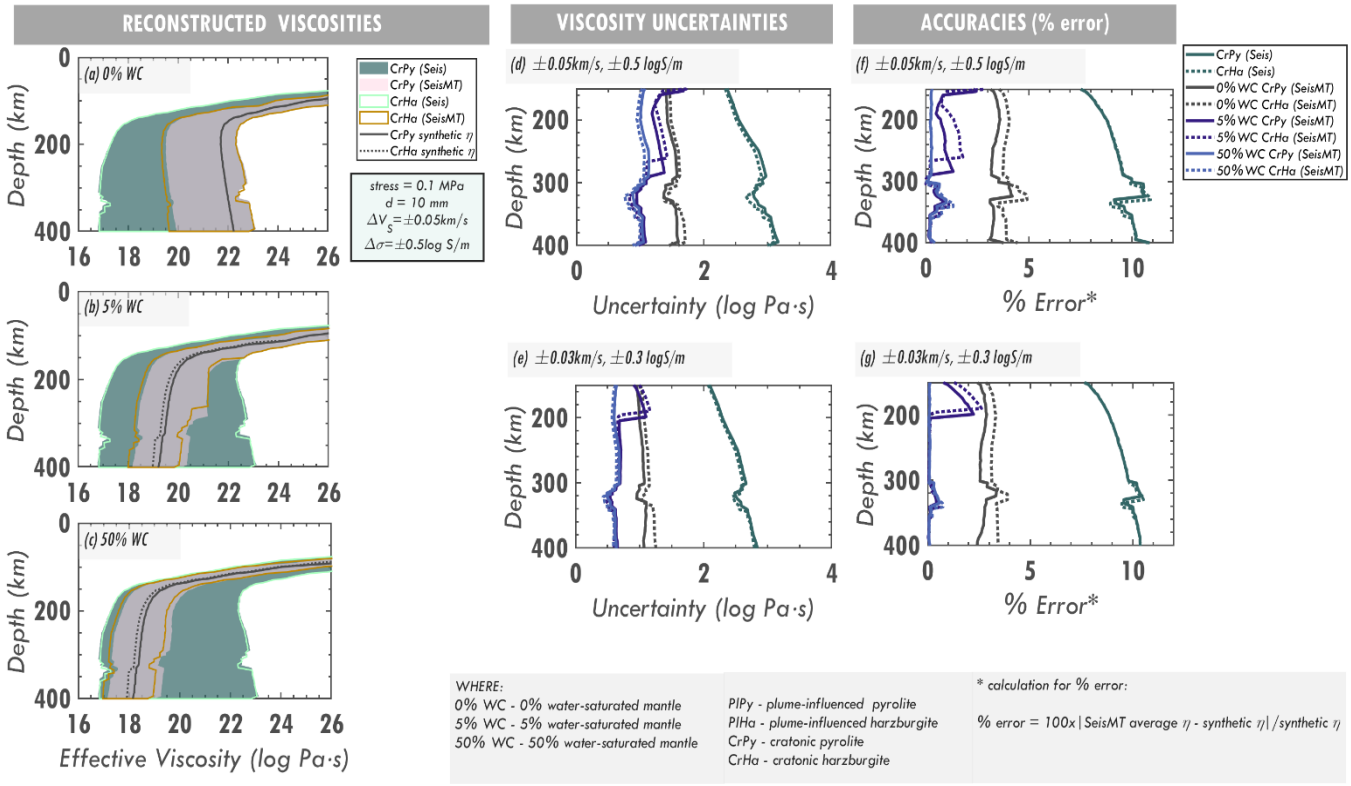

Figure 9. Reconstructed viscosities from seismics only, and both seismics and MT constraints. We employ our method in constructing the viscosity structures (a to c) for different water concentrations (0%, 5%, and 50% WC) for cratonic harzburgite (CrHa) and pyrolite (CrPy) by utilizing the velocities and conductivities in Fig. 6a and b, respectively. The compositional effect is evident, where inferred viscosities are slightly smaller for harzburgite than for pyrolite because it contains more water (a-c). We include different uncertainties on these modelled observations that result in viscosity ranges with different uncertainties (d and e). The viscosities reconstructed using only seismic constraints have large uncertainties (green lines in (d) and (e)) and are less accurate (f and g) because of unconstrained water.

calculating the accuracy of the reconstructed viscosities with respect to their synthetic viscosities (Fig. 9f-g).

Viscosities reconstructed using only seismic constraints (Seis) have large uncertainties ($2-3$ log Pa·s, Fig. 9d-e) due to unconstrained water content. The viscosity uncertainties for pyrolite are larger than for harzburgite because the pyrolite model has slightly larger seismically-inferred temperature ranges (Fig. B, Appendix). When seismic models with smaller velocity uncertainties are available, viscosity uncertainties are reduced (Fig. 9e).

When MT is integrated into our viscosity estimates (SeisMT), the uncertainties of the reconstructed viscosities are much reduced (0.5 – 1.5 log Pa·s) due to well-constrained water contents, and better represent the synthetic viscosities with high accuracy (at most 5% error, Fig. 9f-g). A composition change from pyrolite to harzburgite also affects viscosity uncertainty (compare solid and dashed lines, Fig. 9d-e) due to variations in both water content and temperature ranges. Notably, increasing the bulk water content (say, from 0% to 50% WC) in harzburgite results in a tighter viscosity estimates (by about an order of magnitude), because the MT interpretation shows unambiguously that the upper mantle is wet (Fig. B, Appendix) and thus increases the accuracy of our method (0-1% error). Furthermore, putting tighter bounds on both

MT and seismic observations (small uncertainties) produces tighter viscosity estimates (at half an order of magnitude viscosity uncertainty reduction, Fig. 9e) and improves the accuracy (Fig. 9g) of our method.

7 Discussions

7.1 Limitations and assumptions

In this theoretical investigation, we must select experimental models to convert MT and seismics to temperature and water content, and temperature, water, grain size and stress to viscosity. Although different experimental results exist and some results have significant uncertainties, in practice it has been necessary to select models (e.g., Table 1) in order to convert geophysical observations to mantle properties. While this is a limitation, our method can easily be updated using new or different experimental results. Where multiple experimental constraints exist, we have made conservative choices, including those used to calculate bulk conductivity (Table B, Appendix) within MATE (Özaydin & Selway, 2020) and seismic velocities via Hacker and Abers (2004) and Stixrude and Lithgow-Bertelloni (2005b, 2011). Shear wave velocity computed with HeFESTo (Stixrude and Lithgow-Bertelloni 2005b, 2011) are corrected for attenuation using the spherically averaged 1-D model QR19 (Romanowicz, 1995), which intrinsically includes the different sources of attenuation.

Current experimental data suggest that seismic attenuation is dependent on temperature, seismic frequency, melt and grain size (Faul and Jackson, 2015; Chantel et al., 2016), although precise experimental data quantifying these dependencies are challenging to collect and in some cases are still lacking. We have assumed a melt-free upper mantle for all our calculations, so we do not consider the impact of melt on attenuation. With regard to grain size, experimental data strongly suggest that attenuation due to elastically-accommodated grain boundary sliding increases with decreasing grain size (e.g., Jackson and Faul, 2010) but experiments do not yet accurately constrain the magnitude or frequency range of the associated attenuation peak or its pressure dependence. For this reason we have instead modelled attenuation from seismic observations, without determining the source of attenuation. We do expect that attenuation should be larger for regions with smaller grain sizes at least over some upper mantle depth ranges. If attenuation were not considered in the seismic interpretation particularly at the depths of interest, this decrease in seismic velocity would likely be interpreted as a decrease in viscosity.

We assume that viscosity flow laws for olivine represent the bulk upper mantle viscosity because olivine is the most abundant and well-studied mineral phase. However, the inherent viscosity of other phases such as pyroxenes (e.g., Chen et al., 2006) and the effect of different phases on the overall rheology (e.g., Tasaka et al., 2020; Zhao et al., 2019; Warren & Hirth, 2006; Hansen & Warren, 2015; Bercovici & Skemer, 2017) certainly place errors in this analysis. In principle, such uncertainty could be reduced by employing a viscosity law that incorporates multiple phases. For simplicity, our viscosity calculations are based on the experimental data summarized in Hirth and Kohlstedt (2003) and Ohuchi et al. (2015) and, apart from water, do not include the possible impact of trace and minor element compositions (e.g., Fei et al., 2013; Faul et al., 2016).

We assume three independent major deformation mechanisms in the upper mantle (diffusion creep, dislocation creep and DisGBS), which are assumed to control the effective viscosity calculation

(Eq. 2) as defined by Hirth and Kohlstedt (1996) for constant stress at any depth. We do not consider other mechanisms that may co-exist (i.e., Peierls mechanism which dominates at very high stresses (e.g., Kumamoto et al., 2017; Warren & Hirth, 2006)) or an overall mechanism (phase boundary sliding) that may control the bulk viscosity (Zhao et al., 2019). In principle, all of these factors (multiple phases, minor elements, and other deformation mechanisms) could be incorporated into a more general viscosity law, but the resulting viscosities would have correspondingly larger uncertainty.

Other plausible mantle compositions (e.g., lherzolite or MORB source) and the presence of melt are not considered here for simplicity but would affect seismic velocity, electrical conductivity and viscosity calculations. Also, since water transport into and out of the upper mantle is complicated (e.g., Karato et al., 2020) and not well-constrained, we assume that bulk water content increases with depth in the upper mantle (e.g., Karato, 2012) instead of holding a constant value. This suggests that water in the upper mantle is heterogeneous, with potentially large lateral and radial viscosity variations (Fig. 8f). Thus, we consider a simplified upper mantle with viscosities that are determined by assumed composition, geotherm, bulk water, stress, grain size and geophysical uncertainties. Having good constraints on these parameters from geological and geophysical data will place tighter bounds on viscosity estimates (Fig. 10).

Due to the assumptions and simplifications we have made, we are not making strict interpretations of our results, for instance, about the viscosity uncertainty reduction when MT is added into our analysis. Instead, we explore the factors that control the viscosity, and calculate the resulting viscosity uncertainties and their variations due to the controlling factors, including the geophysical uncertainties. We have not propagated the experimental uncertainties associated with the laboratory-derived parameters into our results, partly because these uncertainties are not always consistently reported. However, our relatively large assumed uncertainties in MT and seismic data are designed to capture some of this experimental uncertainty. Considering a varying geophysical uncertainty along depth would affect the inferred viscosity structures, and therefore the calculated viscosity uncertainties.

7.2 Constraining viscosity estimates

7.2.1 Geophysical constraints and uncertainties

Using both MT and seismic constraints reduces the viscosity uncertainties (≥ 1.5 orders of magnitude; Fig. 10a-c) where the magnitude of reduction depends on the composition and water content (e.g., Fig. 9d), and the geophysical uncertainties involved (Fig. 10c). At shallow depths (< 100 km; Fig. 10a.1), the viscosities estimated from both seismics and MT data are more constrained than when using seismics alone because MT adds additional constraints on the temperature. If we cannot use both MT and seismic constraints (as in the 'not possible' regions in Fig. 3e-i), we have to revisit the geophysical observations, experimental models, composition and other assumptions that we used.

7.2.2 Stress, grain size and deformation mechanism

Constraining grain size and stress certainly improves viscosity estimates (Fig. 10d-f), and the viscosity magnitudes and uncertainties are controlled by the deformation mechanisms (e.g., there

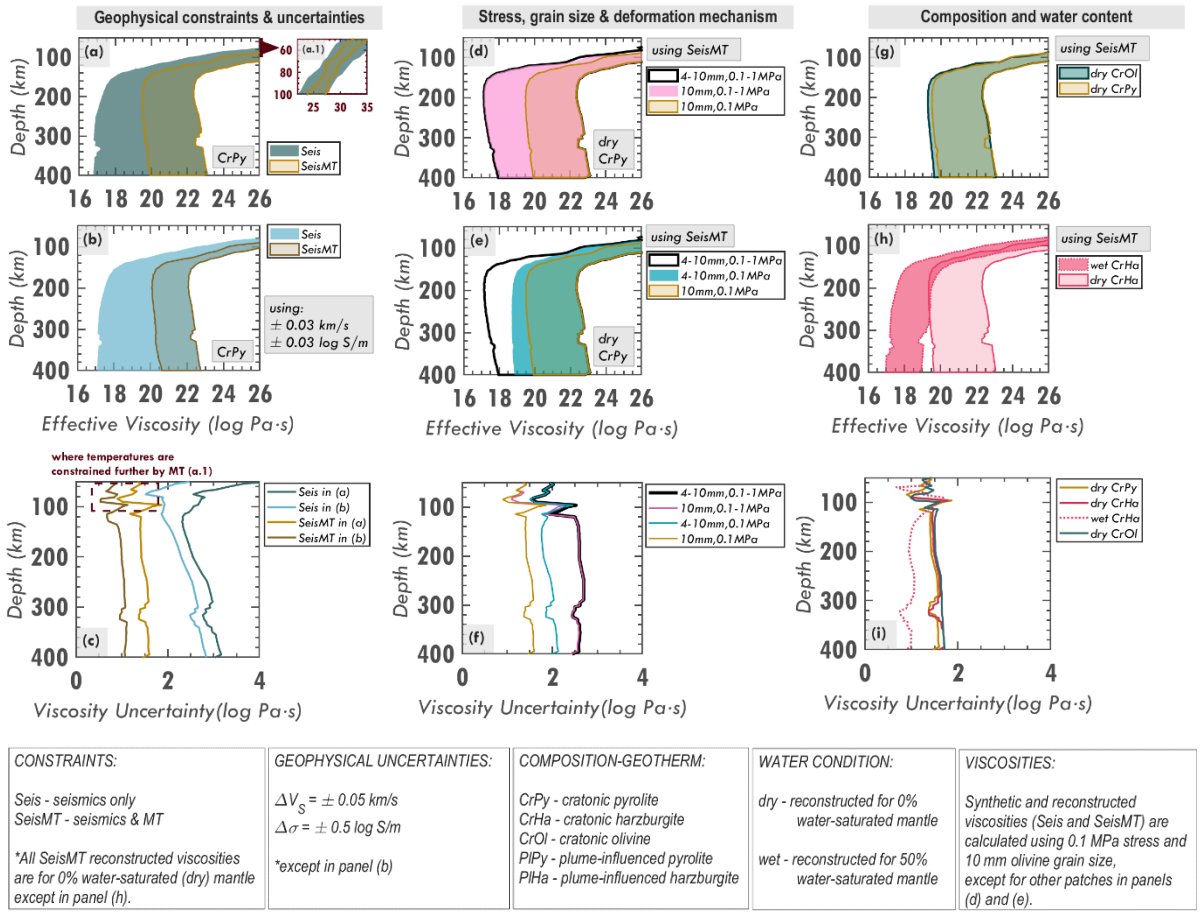

Figure 10. Factors affecting viscosity and its uncertainty. (a-c) Geophysical constraints and their uncertainties. Both seismic and MT constraints improve bounds on the viscosity estimates, thus reducing viscosity uncertainties (brown/yellow lines in (c)), where seismics constrain temperature and MT constrains water. Improving MT and seismic data (e.g., from (b) to (c)) further reduces the viscosity uncertainties (brown line in (c)). **(d-f) Stress, grain size and deformation mechanism.** Using a single choice for stress and grain size constrains the viscosity estimates with smaller uncertainties, (yellow line, (f)) compared to using a wider range of stresses (pink line) and/or grain sizes (blue-green line). **(g-i) Composition and water content.** Variations in composition (green, pink and yellow solid lines in (i)) produce variations in viscosity uncertainties, where knowing a composition apart from pure olivine reduces the viscosity uncertainty. Variations in bulk water content result in variations in viscosity uncertainty (pink solid and dotted lines).

is large uncertainty in the dislocation creep regime). The viscosity uncertainty varies with depth or pressure when multiple deformation mechanisms occur in an upper mantle (Fig. 10f) and is approximately constant when the upper mantle is deforming under a single mechanism. Hence, we can approximate how viscosity would change with depth if we know how the upper mantle is deforming. However, stress and grain size cannot be determined geophysically, so another tool that can provide us a hint about the mechanism would be beneficial. A potential tool for this is seismic anisotropy, which generally can be produced in the dislocation regime but not in the diffusion creep regime (e.g., Hansen et al., 2021), allowing us to distinguish whether the upper mantle is deforming under dislocation creep. This potentially provides information about the grain size that controls the anisotropic structure of the upper mantle by affecting the strain rates of diffusion and dislocation creep (e.g. Behn et al., 2009). However, it is difficult to constrain grain

size geophysically because it evolves with time (e.g., Austin and Evans, 2007), and is affected by deformation history and temperature (e.g., Boneh & Skemer, 2014; Jackson et al., 2002; Jackson et al., 2014). Recent developments in experimental measurements of attenuation by Jackson and Faul (2010) provide an insight on the effects of grain size on attenuation at seismic frequencies and approximately upper mantle temperatures, and provide a potential mechanism to constrain grain size from seismic attenuation measurements. As experimental data and attenuation measurements improve, estimates of upper mantle grain size and therefore viscosity are likely to become more accurate.

7.2.3 Composition, temperature and water

Though composition is not empirically a controlling parameter in the viscosity flow laws we have used, we argue that it is also an important factor in calculating viscosities since it affects the conversion from seismic velocity to temperature and from electrical conductivity to water content (Section 5). Assuming a wrong composition (say pure olivine instead of pyrolite, Fig. 10g) yields a discrepancy in viscosity estimates (Fig. 10i). Such discrepancies could be even larger for compositions with significantly less olivine than those considered in this study. Phase transitions also affect viscosity estimates where temperature and water content may change drastically (e.g.,

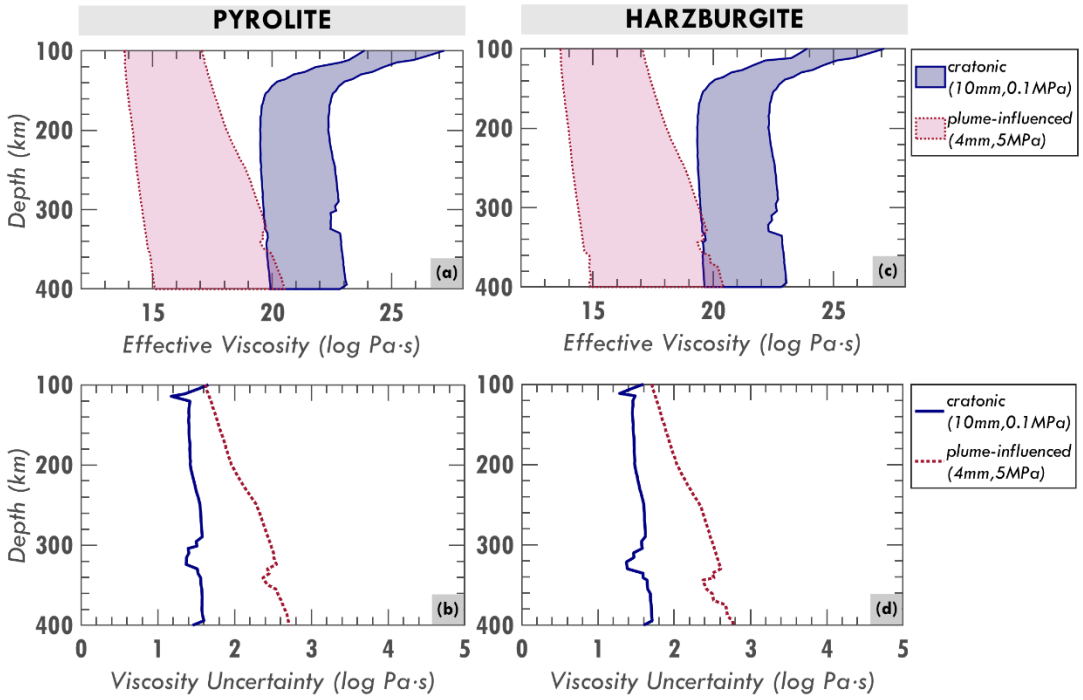

Figure 11. Viscosity estimates for the upper mantle in tectonically stable vs. tectonically active environments. Viscosity structures (a, c) and their associated uncertainties (b, d) for tectonically active environments (hotter, 'plume-influenced' geotherm) and tectonically stable environments (colder, 'cratonic' geotherm), assuming pyrolite and harzburgite compositions, calculated at different grain size and stress combinations. We use the modelled seismic velocities (Fig. 6a) and electrical conductivities for 0% WC (Fig. 6b), and incorporate ±0.05 km/s and ±0.5 log S/m uncertainties, respectively. These geophysical models are converted into temperatures and water concentrations (Figure B, Appendix) which are used to infer viscosity structures (a,c). The plume-influence case is assumed to be tectonically active, with smaller grain sizes (4 mm) and larger stresses (5 MPa) compared to the tectonically stable cratonic environment (10 mm and 0.1 MPa). Viscosity uncertainties are larger for the tectonically active environment, which is controlled by stress-sensitive dislocation creep.

kinks in lines below 290 km, Fig. 10i), which is not evident for a pure olivine assumption. Thus, any other constraints on composition (e.g., xenoliths) will certainly put tighter bounds on viscosity estimates.

As highlighted in previous sections, the calculated viscosity and its associated uncertainty depend on whether the mantle is wet or dry. Dry upper mantle is expected to be more viscous than wet upper mantle (Fig. 10h) and may have larger uncertainties (Fig. 10i). Apart from the viscosity reduction that occurs when water is introduced, the dominant deformation mechanism may also change, which can also affect the inferred viscosity uncertainties. Thus, even in situations where data uncertainties restrict the calculation of a specific water concentration, the general ability of MT to distinguish between a wet and dry upper mantle will provide a significant improvement to viscosity estimates.

Different geotherms produce different viscosity structures and may be associated with significantly different viscosity uncertainties. This variation in viscosity uncertainty may increase by changing the stress and grain size - that is by changing the dominant deformation mechanism (i.e., diffusion to dislocation). Given these observations, we can deduce that a mantle region that may be undergoing active deformation, with a hotter geotherm, smaller grain sizes, and relatively high stresses will have a larger viscosity uncertainty than a stable environment with a colder geotherm, lower stress and larger grain size (Fig. 11).

8 Conclusions

We have developed a method that converts seismic and MT constraints into viscosity structures, accounting for possible compositional effects. Combining both geophysical constraints in viscosity calculations puts tighter bounds on the viscosity estimates compared to considering either one of them alone. Having good quality MT and seismic data with small uncertainties can further improve the viscosity estimates. MT can distinguish whether an upper mantle is wet or dry, which greatly helps to reduce viscosity uncertainty. Thus, more MT surveys in environments where we want to have good viscosity structures (e.g., polar regions) would improve robust geodynamic and GIA modelling. For example, applying this method in places where currently only seismic observations are used (e.g.., Heezsel et al., 2016; Milne et al., 2018; Lucas et al., 2020) would improve viscosity estimates. It could also be employed, for example, in Fennoscandia where viscosities are well constrained by GIA (e.g., Lambeck et al., 1998; Milne et al., 2001; Kierulf et al., 2014) to evaluate the viscosity structures obtained using this method. In addition, having a good knowledge of stress, grain size and composition can further improve the viscosity estimates (by more than an order of magnitude). Stress and grain size control the deformation regime (dislocation vs. diffusion creep, and grain-boundary sliding), which affects both the viscosity and its associated uncertainty. Composition directly affects seismic velocities and electrical conductivities, which are the constraints used in our method, and thus affects the output viscosities. For instance, we observe a trade-off between composition and temperature when estimating viscosity from seismic data. This can lead to an incorrect interpretation of both thermal and viscosity structures of mantle rocks if velocity variations are assumed to be only thermally controlled. Given these results, our method should help to improve estimates of mantle viscosity, and its uncertainty, for both tectonically active and stable environments (Fig. 11), as long as the upper mantle is geophysically well-characterized by seismic and magnetotelluric observations.

Acknowledgments

This work was supported partly by the Research Council of Norway's projects 223272 (Centre of Excellence) and 288449 (MAGPIE Project), and partly by the Australian Research Council grant FT150100541, and the Louis B. and Martha B. Slichter Geoscience Chair funds.

Open Research

Data Availability Statement

The generated datasets are not archived in a repository since they are reproducible using the online softwares summarized in the Software Availability Statement.

Software Availability Statement

The thermodynamic simulation package HeFESTo (Stixrude and Lithgow-Bertelloni, 2005b and 2011) is available at https://github.com/stixrude/HeFESToRepository. The parameter set is at https://github.com/stixrude/HeFESTo_Parameters_251010. The MATE software (Özaydin & Selway, 2020) is available at https://github.com/sinanozaydin/MATE, and the models chosen are summarized in Table B (Appendix). The excel file of Hacker and Abers (2004) is in their supplementary information.

Appendix

A. Geotherm calculation

The constructed plume-influenced and cratonic geotherms (Fig. 6c) represent two-end member cases that bracket a range of upper mantle states. The lithospheric component of both geotherms is calculated using equation 4.31 of Turcotte and Schubert (2014), which is:

$$T_{lith}(z) = T_0 + \frac{q_m}{k} z + \frac{(q_m - q_0) h_r}{k} \left(1 - e^{-\frac{z}{h_r}}\right) \quad \text{(A.1)}$$

where z is depth, $k = 3.35$ Wm^{-1}K^{-1} is the thermal conductivity, $h_r = 20$ km is the length scale for crustal radioactivity, q_0 is the surface heat flux and q_m is the mantle heat flux. The q_0 and q_m used for plume-influenced and cratonic geotherms are summarized in Table A.

Below lithosphere, we define the mantle adiabat as:

$$T_{um}(z) = T_p + \gamma z \quad \text{(A.2)}$$

where T_p is the potential temperature of the adiabat at the surface (Table A) and $\gamma = \left(\frac{\partial T}{\partial z}\right)_S$ is the adiabatic temperature gradient. We use $\gamma = 0.4$ K/km from Katsura et al. (2010).

We combine the above equations to form an overall geotherm using:

$$T(z) = min(T_{lith}, T_{um}) - (200\text{°C}) \frac{300\text{°C}}{300\text{°C} + |T_{lith} - T_{um}|} \quad \text{(A.3)}$$

where the (arbitrary) second term is included merely to smooth the transition between the two curves near their intersection.

Table A. Parameters used in constructing different geotherms and Models and assumptions used in MATE software to calculate electrical conductivity and water.

Parameters/ Geotherm	**Cratonic**	**Plume-influenced**
T_p(℃)	1350	1450
$q_m(mW/m^2)$	30	70
$q_0(mW/m^2)$	50	90
MATE Entry	**Model**	
Composition Entry:		
for Al_2O_3	*Calculated using (Özaydin & Selway, 2020)* $C_{al}^{opx} = 0.92654 + 4.69\ exp(-1.24012P)$	
Fe fractions	*0.10*	
Composition set-up:		
Al-dependency	*SAF Archon/Proton-Archon Xenoliths*	
Water Partitioning:	Px handled independently	
Opx/Ol	*Type 4 – Demouchy 2017 average single value of opx/ol at 3 GPa and 1373 K with aluminous-opx-cpx-ol-gt assemblage*	
Cpx/Ol	*Type 5 – Cpx-opx dependent cpx/ol values from P-dependent function*	
Water Solubility:		
Ol	*PadronNavarta2017*	
Conductivity Models:		
Ol	*Gardes2014*	
Opx	*Dai2009*	
Cpx	*Liu2019*	
Gt	*Dai2009a*	
Amp	*Hu2018H*	
Phlg	*Li2016*	

B. Temperature and water content inferred from seismics and MT

We consider the forward-calculated shear wave velocities in Fig. 6a for both harzburgite and pyrolite for plume-influenced and cratonic geotherms (Fig 6c) calculated in Section A. Then we attempt to reconstruct the thermal structures from the forward modelled shear wave velocities with the assumption that we know the compositions (harzburgite and pyrolite) and by assuming a constant velocity uncertainty along depth that translates into temperature uncertainties (Fig. B(i)). Next, we try to determine the water contents (bulk and in olivine phase only) at depth using the inferred thermal structures and the forward-calculated electrical conductivities (Fig. 6b) with constant uncertainty using the MATE software. To do this, we utilize the phase proportions (Fig. 5) and the thermal structures as inputs into MATE. Then we uploaded into the MATE software the forward-modelled electrical conductivity structures (with uncertainty) assuming different bulk water contents (0%, 5% and 50% WC) as synthetic MT data, and let the software solve for the water contents (Fig. B(ii) to (vii)) using the chosen models in Table A. Due to the uncertainties included in this calculation, at any given temperature and depth, there is a range of water contents that can produce the desired conductivity range (as in Fig. 2b). Thus, we need to determine the water content ranges for lower (ii, iv, vi) and upper (iii, v, vii) temperature bounds separately. The seismically-inferred temperatures are constrained further by MT, particularly at shallow depths.

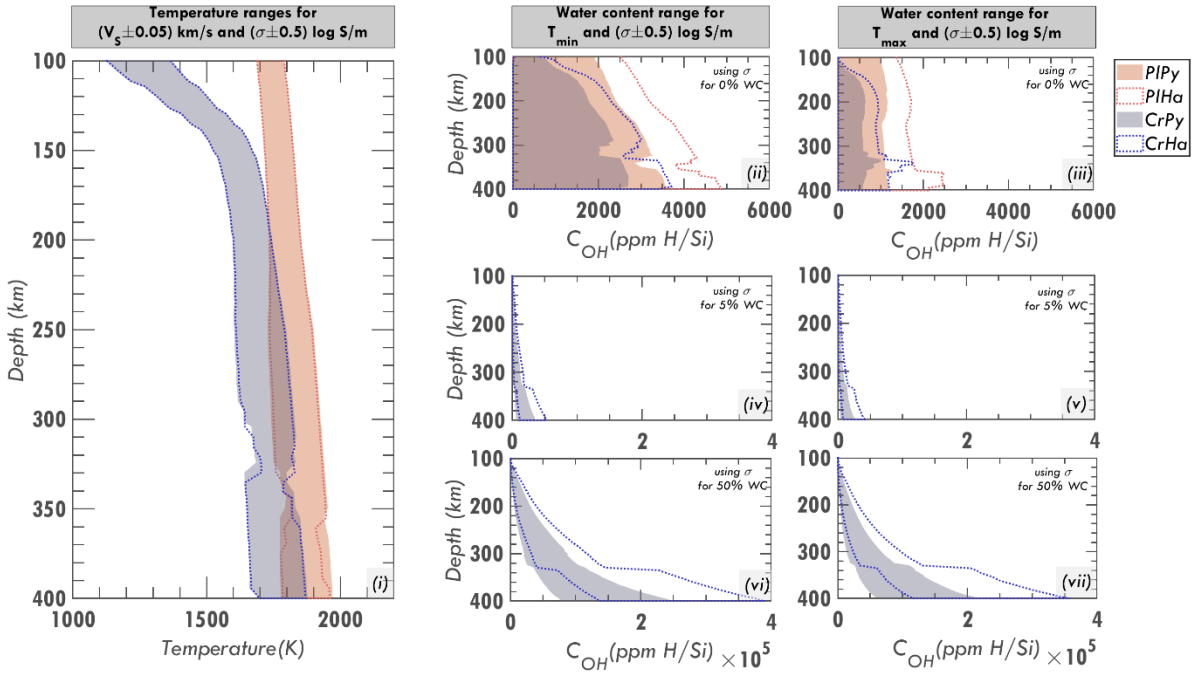

Figure B. Constrained temperatures (i) and water contents in olivine (ii-vii) from seismic and MT data. The velocity uncertainty (±0.05 km/s) used in the calculation translates into temperature uncertainty, producing a thermal structure with lower temperature bound (T_{min}) and upper temperature bound (T_{max}). The inferred thermal structures are further constrained when MT data is integrated (compare panel (i) with Fig. 7b). From the electrical conductivity structures (with assumed ±0.5 log S/m uncertainty), the ranges of water content in olivine phase for harzburgite (dashed-edge colorless patches) and pyrolite (colored patches) are calculated for lower (ii, iv, vi) and upper temperature bounds (iii, v, vii) using MATE software.

Notably, the thermal structures for harzburgite are slightly tighter than those for pyrolite, but the water contents of harzburgite are significantly larger than pyrolite.

References

Artemieva, I. (2006), Global 1x1 thermal model TC1 for the continental lithosphere: Implications for lithosphere secular evolution. *Tectonophysics, 416*, 245-277.

Austin, N.J., & Evans, B. (2007), Paleowattmeters: A scaling relation for dynamically recrystallized grain size. *Geology, 35*, 343-346.

Ave Lallemant, H., Mercier, J.-C., Carter, N., & Ross, J. (1980), Rheology of the upper mantle: Inferences from peridotite xenoliths. *Tectonophysics, 70*, 85-113. doi:https://doi-org.ezproxy.uio.no/10.1016/0040-1951(80)90022-0

Bell et al., (2003), Hydroxide in olivine: A quantitative determination of the absolute amount and calibration of the IR spectrum. *Journal of Geophysical Research, 108*. doi:10.1029/2001JB000679

Bercovici, D., & Ricard, Y. (2012), Mechanisms for the generation of plate techtonics by two-phase grain-damage and pinning. *Physics of the Earth and Planetary Interiors, 202-203*, 27-55.

Chantel, J., Manthilake, G., Andrault, D., Novella, D., Yu, T., & Wang, Y. (2016), Experimental evidence supports mantle partial melting in the asthenosphere. *Science Advances, 2*, e1600246.

Chen, S., Hiraga, T., & Kohlstedt, D. L. (2006), Water weakening of clinopyroxene in the dislocation creep regime. *Journal of Geophysical Research, 111*, B08203. doi:10.1029/2005JB003885

Conrad, C. P. (2013), The solid Earth's influence on sea level. *Geol. Soc. Am. Bullet., 125*, 1027-1052.

Conrad, C., & Hager, B. (1997), Spatial variations in the rate of sea level rise caused by the present-day melting of glaciers and ice sheets. *Geophysical Research Letters, 24*(12), 1503-1506. doi:10.1029/97gl01338

Conrad, C., & Lithgow-Bertelloni, C. (2006), Influence of continental roots and asthenosphere on plate-mantle coupling. *Geophysical Research Letters, 33*(L05312), 1-4. doi:10.1029/2005GL025621

Courtier, A., Bagley, B., and Revenaugh, J. (2007), Whole mantle discontinuity structure beneath Hawaii. *Geophys. Res. Lett., 34*, L17304. doi:10.1029/2007GL031006

Dalton, C., & Ekström, G. (2006a), Global models of surface-wave attenuation. *J. Geophys. Res., 111*, B05317. doi:10.1029/2005JB003997

Dalton, C., Ekström, G. & Dziewonski, A. (2008), The global attenuation structure of the upper mantle. *J. Geophys. Res., 113*, B09303. doi:10.1029/2007JB005429

Debayle, E., Bodin, T., Durand, S. & Ricard, Y. (2020), Seismic evidence for partial melt below tectonic plates. *Nature, 586*, 555-559. doi:10.1038/s41586-020-2809-4

Faul, U., & Jackson, I. (2005), The seismological signature of temperature and grain size variations in the upper mantle. *Earth and Planetary Science Letters, 234*, 119-134. doi:10.1016/j.epsl.2005.02.008

Faul, U., & Jackson, I. (2015), Transient Creep and Strain Energy Dissipation: An Experimental Perspective. *Annu. Rev. Earth Planet. Sci., 43*, 541-569. doi:10.1146/annurev-earth-060313-054732

Faul, U., Cline II, C., David, E., Berry, A., & Jackson, I. (2016), Titanium-hydroxyl defect-controlled rheology of the Earth's upper mantle. *Earth and Planetary Science Letters, 452*, 227-237.

Fei, H., Wiedenbeck, M., Yamazaki, D., & Katsura, T. (2013), Small effect of water on upper-mantle rheology based on silicon self-diffusion coefficients. *Nature, 498*, 213-215. doi:10.1038/nature12193

Forte, A., & Mitrovica, J. (2001), Deep-mantle high-viscosity flow and thermochemical structure inferred from seismic and geodynamic data. *Nature, 410*, 1049-1056. doi:https://doi.org/10.1038/35074000

Forte, A., & Peltier, R. (1994), The Kinematics and Dynamics of Poloidal-Toroidal Coupling in Mantle Flow: The Importance of Surface Plates and Lateral Viscosity Variations. *Advances in Geophysics, 36*, 1-119.

Fullea, J., Lebedev, S., Martinec, Z., & Celli, N. L. (2021), WinterC-G: mapping the upper mantle thermochemical heterogeneity from coupled geophysical-petrological inversion of seismic waveforms, heat flow, surface elevation and gravity satellite data. Geophysical Journal International, 226, 146-191. doi:10.1093/gji/ggab094

Gardés, E., Gaillard, F., & Tarits, P. (2014), Toward a unified hydrous olivine electrical conductivity law. *Geochem. Geophys. Geosyst., 15*, 4984-5000. doi:10.1002/2014GC005496

Glover, P. W. (2010), A generalized Archie's law for n phases. *Geophysics, 75*(6), E247-E265. doi:10.1190/1.3509781

Goes, S., Govers, R., & Vacher, P. (2000), Shallow mantle temperatures under Europe from P and S wave tomography. *Journal of Geophysical Research, 105*, 11153-11169.

Hacker, B., & Abers, G. (2004), Subduction Factory 3: An Excel worksheet and macro for calculating the densities, seismic wave speeds, and H2O contents of minerals and rocks at pressure and temperature. *Geochemistry, Geophysics, Geosystems*, Q01005. doi:10.1029/2003GC000614

Hansen, L., & Warren, J. (2015), Quantifying the effect of pyroxene on deformation of peridotite in a natural shear zone. *JGR Solid Earth, 120*(4), 2717-2738. doi:10.1002/2014JB011584

Hansen, L., Faccenda, M., & Warren, J. (2021), A review of mechanisms generating seismic anisotropy in the upper mantle. *Physics of the Earth and Planetary Interiors, 313*, 106662. doi:10.1016/j.pepi.2021.106662

Heeszel, D., D., W., Anandakrishnan, S., Aster, R., Dalziel, I., Huerta, A., . . . Winberry, J. (2016), Upper mantle structure of central and West Antarctica from array analysis of Rayleigh wave phase velocities. *J. Geophys. Res. Solid Earth, 121*, 1758-1775. doi:10.1002/2015JB012616

Hirth, G., & Kohlstedt, D. (1996), Water in the oceanic upper mantle: implications for rheology, melt extraction and the evolution of the lithosphere. *Earth and Planetary Science Letters, 144*, 93-108.

Hirth, G., & Kohlstedt, D. (2003), Rheology of the Upper Mantle and the Mantle Wedge: A View from the Experimentalists. *Inside the Subduction Factory, Geophysical Monograph, 138*, 83-105.

Ivins, E., & Sammis, C. (1995), On lateral viscosity contrast in the mantle and the rheology of low-frequency geodynamics. *Geophys. J. Int., 123*, 305-322.

Ivins, E. R., van der Wal, W., Wiens, D. A., Lloyd, A. J., and Caron, L. (2021), Antarctic upper mantle rheology. In: Martin, A. P. and van der Wal, W. (eds) The Geochemistry and Geophysics of the Antarctic Mantle. Geological Society, London, Memoirs, 56, https://doi.org/10.1144/M56-2020-19

Jackson, I., & Faul, U. (2010), Grainsize-sensitive viscoelastic relaxation in olivine: Towards a robust laboratory-based model for seismological application. *Physics of the Earth and Planetary Interiors, 183*, 151-163. doi:10.1016/j.pepi.2010.09.005

Jackson, I., Faul, U., & Skelton, R. (2014), Elastically accommodated grain-boundary sliding: New insights from experiment and modeling. *Physics of the Earth and Planetary Interiors, 228*, 203-210. doi:10.1016/j.pepi.2013.11.014

Jackson, I., Fitz Gerald, J., Faul, U., & Tan, B. (2002), Grain-size-sensitive seismic wave attenuation in polycrystalline olivine. *J. Geophys. Res., 107*(B12), 2360. doi:10.1029/2001JB001225

Jacobsen, S. D., Jiang, F., Mao, Z., Duffy, T. S., Smyth, J. R., Holl, C. M., Frost, D. J. (2008), Effects of hydration on the elastic properties of olivine. *Geophys. Res. Lett., 35*, L14303. doi:10.1029/2008GL034398.

Johnston, P., Wu, P. & Lambeck, K. (1998), Dependence of horizontal stress magnitude on load dimension in glacial rebound models. *Geophys. J. Int. 132*, 41-60. https://doi.org/10.1046/j.1365-246x.1998.00387.x

Karato, S.-i (2012), On the origin of asthenosphere. *321-322*, 95-103. doi:10.1016/j.epsl.2012.01.001

Karato, S.-i., & Jung, H. (1998), Water, partial melting and the origin of the seismic low velocity and high attenuation zone in the upper mantle. *Earth and Planetary Science Letters, 157*, 193-207.

Karato, S.-i., & Jung, H. (2003), Effects of pressure on high-temperature dislocation creep in olivine. *Philosophical Magazine, 83*, 401-414.

Karato, S.-i., & Karki, B. (2001), Origin of lateral variation of seismic wave velocities and density in the deep mantle. *Journal of Geophysical Research, 106*(B10), 21771-21783.

Karato, S.-i., & Wu, P. (1993), Rheology of the Upper Mantle: A Synthesis. *Science, 260*, 771-778.

Karato, S.-i., Karki, B., Park, J. (2020), Deep mantle melting, global water circulation and its implications for the stability of the ocean mass. *Prog Earth Planet Sci, 7*, 76. https://doi.org/10.1186/s40645-020-00379-3

Karato, S.-i., Rubie, D., & Yan, H. (1993), Dislocation Recovery in Olivine Under Deep Upper Mantle Conditions: Implications for Creep and Diffusion. *Journal of Geophysical Research, 98*, 9761-9768.

Katsura, T., Yoneda, A., Yamazaki, D., Yoshino, T., & Ito, E. (2010), Adiabtic tempertaure profile in the mantle. *Physics of the Earth and Planetary Interiors, 183*, 212-218. doi:10.1016/j.pepi.2010.07.001

Kaufmann, G., & Lambeck, K. (2000), Mantle dynamics, postglacial rebound and the radial viscosity profile. *Physics of the Earth and Planetary Interiors, 121*, 301-324.

Khan, S. A., Sasgen, I., Bevis, M., van Dam, T., Bamber, J., Wahr, J., . . . Munneke, P. K. (2016), Geodetic measurements reveal similarities between post-Last Glacial Maximum and present-day mass loss from the Greenland ice sheet. *Science Advances, 2*(9). doi:10.1126/sciadv.1600931

Kierulf, H., Steffen, H., Simpson, M., Lidberg, M., Wu, P., & Wang, H. (2014), A GPS velocity field for Fennoscandia and a consistent comparison to glacial isostatic adjustment models. *J. Geophys. Res. Solid Earth, 119*, 6613-6629. doi:10.1002/2013JB010889

Lambeck, K., Smither, C., & Johnston, P. (1998), Sea-level change, glacial rebound and mantle viscosity for northern Europe. *Gephys. J. Int., 134*, 102-144.

Lebedev, S., Boonen, J., & Trampert, J. (2009), Seismic structure of Precambrian lithosphere: New constraints from broad-band surface-wave dispersion. *Lithos, 109*, 96-111. doi:10.1016/j.lithos.2008.06.010

Lee, C.-T. A. (2003), Compositional variation of density and seismic velocities in natural peridotites at STP conditions: Implications for seismic imaging of compositional heterogeneities in the upper mantle. *J. Geophys. Res., 108*(B9), 2441. doi:doi:10.1029/2003JB002413

Liu, L., & Hasterok, D. (2016), High-resolution lithosphere viscosity and dynamics revealed by magnetotelluric imaging. *Science, 353*, 1515-1519. doi:10.1126/science.aaf6542

Lucas, E., Soto, D., A., N., Llyod, A., Aster, R., Wiens, D., et al. (2020), P- and S-wave velocity structure of central West Antarctica: Implications for the tectonic evolution of the West Antarctic Rift System. *Earth and Planetary Science Letters, 546*, 116437. doi:10.1016/j.epsl.2020.116437

Mei, S., & Kohlstedt, D. L. (2000a), Influence of water on plastic deformation of olivine aggregates: 1. Diffusion creep regime. *Journal of Geophysical Research, 105*, 21457-21469.

Mei, S., & Kohlstedt, D. L. (2000b), Influence of water on plastic deformation of olivine aggregates: 2. Dislocation creep regime. *J. Geophys. Res., 105*, 21471-21481.

Milne, G., Davis, J., Mitrovica, J., Scherneck, H.-G., Johansson, J., Vermeer, M., & Koivula, H. (2001), Space-Geodetic Constraints on Glacial Isostatic Adjustment in Fennoscandia. *Science, 291*, 2381-2385.

Milne, G., Latychev, K., Schaeffer, A., Crowley, J., Lecavalier, B., & Audette, A. (2018), The influence of lateral Earth structure on glacial isostatic in Greenland. *Geophysical Journal International, 214*(2), 1252-1266. doi:10.1093/gji/ggy189

Mitrovica, J. X., Tamisiea, M. E., Davis, J. L., & Milne, G. A. (2001), Recent mass balance of polar ice sheets inferred from patterns of global sea-level change. *Nature, 409*(6823), 1026-1029. doi:10.1038/35059054

Mitrovica, J., & Forte, A. (1997), Radial profile of mantle viscosity: Results from the joint inversion of convection and postglacial rebound observables. *Journal of Geophysical Research, 102*, 2751-2769.

O'Donnell, J., Selway, K., Nyblade, A., Brazier, R., Wiens, D., Anandakrishnan, S., . . . Winberry, J. (2017), The uppermost mantle seismic velocity and viscosity structure of central West Antarctica. *Earth and Planetary Science Letters, 472*, 38-49.

Ohuchi, T., Kawazoe, T., Higo, Y., Funakoshi, K.-i., Suzuki, A., Kikegawa, T., & Irifune, T. (2015), Dislocation-accommodated grain boundary sliding as the major deformation mechanism of olivine in the Earth's upper mantle. *Science Advances, 1*, 1-10.

Özaydin, S., & Selway, K. (2020), MATE: An Analysis Tool for the Interpretation of Magnetotelluric Models of the Mantle. *Geochemistry, Geophysics, Geosystems, 21*, 1-26. doi:10.1029/2020GC009126

Padrón-Navarta, J., & Hermann, J. (2017), A Subsolidus Olivine Water Solubility Equation for the Earth's Upper Mantle. *Journal of Geophysical Research: Solid Earth, 122*, 9862-9880. doi:10.1002/2017JB014510

Paulson, A., Zhong, S., & Wahr, J. (2005), Modelling post-glacial rebound with lateral viscosity variations. *Geophys. J. Int., 163*, 357-371. doi:10.1111/j.1365-246X.2005.02645.x

Paulson, A., Zhong, S., & Wahr, J. (2007), Limitations on the inversion for mantle viscosity from postglacial rebound. *Geophys. J. Int., 168*, 1195-1209. doi:10.1111/j.1365-246X.2006.03222.x

Peltier, W. (2004), Global Glacial Isostasy and the Surfac eof the Ice-Age Earth: The ICE-5G (VM2) Model and GRACE. *Annu. Rev. Earth Planet. Sci., 32*, 111-149.

Peltier, W., Farrell, W., & Clark, J. (1978), Glacial Isostasy and Relative Sea Level: A Global Finite Element Model. *Tectonophysics, 50*, 81-110.

Peslier, A., Schönbächler, M., Busemann, H., & Karato, S.-I. (2017), Water in the Earth's Interior: Distribution and Origin. *Space Sci Rev, 212*, 743-810. doi:10.1007/s11214-017-0387-z

Pollitz, F., Banerjee, P., Grijalva, K., Nagarajan, B., & Bürgmann, R. (2008), Effect of 3-D viscoelastic structure on post-seismic relaxation from the 2004 M=9.2 Sumatra earthquake. *Geophys. J. Int., 173*, 189-204. doi:10.1111/j.1365-246X.2007.03666.x

Pollitz, F., Peltzer, G., & Bürgmann, R. (2000), Mobility of continental mantle: Evidence from postseismic geodetic observations following the 1992 Landers earthquake. *Journal of Geophysical Research, 105*, 8035-8054.

Richards, M. A., W.-S. Yang, J. R. Baumgardner, and H.-P. Bunge (2001), Role of a low-viscosity zone in stabilizing plate tectonics: Implications for comparative terrestrial

890 planetology, Geochemistry, Geophysics, Geosystems, 2(8), 1026,
891 doi:10.1029/2000GC000115.
892 Romanowicz, B. (1995), A global tomographic model of shear attenuation in the upper mantle. J.
893 Geophys. Res., 100, 12,375-12,394.
894 Selway, K. (2015), Negligible effect of hydrogen content on plate strength in East Africa. *Nature*
895 *Geoscience, 8*, 543-546.
896 Selway, K., & O'Donnell, J. (2019), A small, unextractable melt fraction as the cause for the low
897 velocity zone. *EPSL, 517*, 117-124. doi:10.1016/j.epsl.2019.04.012
898 Selway, K., Smirnov, M. Y., Beka, T. O., Minakov, A., SEnger, K., Faleide, J. I., & Kalscheuer,
899 T. (2020), Magnetotelluric Constraints on the Temperature, Composition, Partial Melt
900 Content, and Viscosity of the Upper Mantle Beneath Svalvard. *Geochemistry,*
901 *Geophysics, Geosystems, 21*, 1-12.
902 Shen, W., Wiens, D., Anandakrishnan, S., Aster, R., Gerstoft, P., Bromirski, P., . . . Heeszel, D.
903 (2018), The Crust and the Upper Mantle Structure of Central and West Antarctica From
904 Bayesian Inversion of Rayleigh Wave and Receiver Functions. *J. Geophys. Res.: Solid*
905 *Earth, 123*, 7824-7849. doi:10.1029/2017JB015346
906 Stevens, N., Parizek, B., & Alley, R. (2016), Enhancement of volcanism and geothermal heat
907 flux by ice-age cycling: A stress modeling study of Greenland. *J. Geophys. Res. Earth*
908 *Surf., 121*, 1456-1471. doi:10.1002/2016JF003855
909 Stixrude, L., & Lithgow-Bertelloni, C. (2005a), Mineralogy and elasticity of the oceanic upper
910 mantle: Origin of the low-velocity zone. *J. Geophys. Res., 110*, B03204,
911 doi:10.1029/2004JB002965.
912 Stixrude, L., & Lithgow-Bertelloni, C. (2005b), Thermodynamics of mantle minerals - I.
913 Physical properties. *Geophys. J. Int., 162*, 610-632. doi:10.1111/j.1365-
914 246X.2005.02642.x
915 Stixrude, L., & Lithgow-Bertelloni, C. (2011), Thermodynamics of mantle minerals - II. Phase
916 equilibria. *Geophys. J. Int., 184*, 1180-1213. doi:10.1111/j.1365-246X.2010.04890.x
917 Turcotte, D., & Schubert, G. (2014), *Geodynamics* (3rd ed.). New York: Cambridge University
918 Press.
919 Wang, D., Mookherjee, M., Xu, Y., & Karato, S. (2006), The effect of water on the electrical
920 conductivity of olivine. *Nature*, *443*(26), 977-980. doi:10.1038/nature05256
921 Wang, K., Hu, Y., & He, J. (2012), Deformation cycles of subduction earthquakes in a
922 viscoelastic Earth. *Nature, 484*, 327-332.
923 Xu, W., Lithgow-Bertelloni, C., Stixrude, L., & Ritsema, J. (2008), The effect of bulk
924 composition and temperature on mantle seismic structure. *Earth and Planetary Science*
925 *Letters, 275*, 70-79.
926 Yoshino, T., Matsuzaki, T., Shatskiy, A., & Katsura, T. (2009), The effect of water on the
927 electrical conductivity of olivine aggregates and its implications for the electrical
928 structure of the upper mantle. *Earth and Planetary Science Letters, 288*, 291-300.
929 doi:10.1016/j.epsl.2009.09.032
930 Zhao, Y.-H., Ginsberg, S. B., & Kohlstedt, D. L. (2004), Solubility of hydrogen in olivine:
931 dependence on temperature and iron content. *Contrib. Mineral. Petrol. 147*, 155-161.
932 doi:10.1007/s00410-003-0524-4
933 Zhao, N., Hirth, G., Cooper, R., Kruckenberg, S., & Cuckjati, J. (2019), Low viscosity of mantle
934 rocks linked to phase boundary sliding. *EPSL, 517*, 83-94.
935 doi:10.1016/j.epsl.2019.04.019